A PIXELIZED GALLIUM ARSENIDE RADIATION DETECTOR

by

David George Webster

B. Sc. (Hon) (Physics) University of Victoria

A THESIS SUBMITTED IN PARTIAL FULFILLMENT OF

THE REQUIREMENTS FOR THE DEGREE OF

MASTER OF SCIENCE

in the Department

of

PHYSICS

© DAVID GEORGE WEBSTER 1988

SIMON FRASER UNIVERSITY

August 1988

All rights reserved. This work may not be

reproduced in whole or in part, by photocopy

or other means, without permission of the author.

APPROVAL

NAME: David George Webster

DEGREE: Master of Science

TITLE OF THESIS: A Pixelized Gallium Arsenide Radiation Detector

EXAMINING COMMITTEE:

Chairman: Professor Michael Thewalt

____

Professor Otto Haüsser
Senior Supervisor

____

John Cresswell
Engineer, TRIUMF

____

Roy Morrison
Professor

____

Professor Richard R. Johnson
External Examiner
Department of Physics, University of British Columbia

Date approved Aug. 15 /88

PARTIAL COPYRIGHT LICENSE

I hereby grant to Simon Fraser University the right to lend my thesis, project or extended essay (the title of which is shown below) to users of the Simon Fraser University Library, and to make partial or single copies only for such users or in response to a request from the library of any other university, or other educational institution, on its own behalf or for one of its users. I further agree that permission for multiple copying of this work for scholarly purposes may be granted by me or the Dean of Graduate Studies. It is understood that copying or publication of this work for financial gain shall not be allowed without my written permission.

Title of Thesis/Project/Extended Essay

A Pixelized Gallium Arsenide Radiation Detector

Author: ______

(signature)

David George Webster

(name)

Aug 18, 88

(date)

Acknowledgement

I would like to thank TRIUMF, NSERC, and Otto Haüsser for their financial support over the past two years, and also the many other people who have helped both directly and indirectly with this work, particularly members of the microelectronics group at TRIUMF. Especially I would like to thank John Cresswell and Maurice LeNoble for teaching me the ins and outs of electronics and device processing.

Table of Contents

Abstract iii

Acknowledgement iv

1 Introduction 1

1.1 Particle Detectors and Detector Interactions 1

1.2 Signal Charge Production 6

2 Proposal 9

3 Device Design 11

3.1 Why Epitaxial GaAs? 11

3.2 Difficulties With GaAs 12

3.3 The TRIUMF Pixelized GaAs Detector (TPGD) 14

3.4 Device Considerations 17

3.5 Computer Modelling 19

3.5.1 The RELAX3D Program 19

3.5.2 The Modelled Sections 21

3.5.3 Predetermined, Fixed Charge Distributions 23

3.5.4 Results 24

4 Fabrication of the TRIUMF Pixelized GaAs Detector (TPGD) 40

5 Electrical Measurements 43

5.1 Fabrication Stage 43
5.2 Post-Bonding Stage 44
5.3 TPGD Operating Conditions 45

6 Amplifiers and Data Collection **48**
6.1 Charge Preamplifier Circuits 51
6.2 Voltage Preamplifier Circuit 57
6.3 Data Acquisition Systems 57

7 Radiation Detection **61**
7.1 Alpha Particles 61
7.2 Ruthenium Electrons 68
7.3 Protons and Pions 71
7.3.1 Data Collection 71
7.3.2 Results 72

8 Conclusion **81**
8.1 Alpha Particles 81
8.2 Protons and Pions 82
8.3 Summary 82

A Fabrication Routine **83**

B Design Calculations **86**
B.1 Epitaxial Layer Thickness 86
B.2 Signal Size 88
B.3 Structure Capacitance 89
B.4 Response Time 94

B.5 Noise Sources 95
B.5.1 Johnson noise 95
B.5.2 Dark Current 96
B.5.3 Generation Current 96
B.6 Straggling 98
B.7 Pion Energy Deposition 98

Bibliography **99**

List of Tables

3.1 Boundary conditions for Laplace problem. 25

3.2 Boundary conditions for Poisson problems. 30

5.3 Leakage current criteria for the TPGD. 44

7.4 Alpha energy as a function of air spacing. 63

7.5 Charge collected in the TPGD for incident alpha particles. 67

B.6 Depletion depths for various doping densities and voltages 88

B.7 Capacitance of coplanar plates with and without fringing fields. 94

List of Figures

1.1 Time constants for different recombination modes 8

3.2 Charge collection by drift parallel to the surface. 14

3.3 TPGD layout. 16

3.4 Modelled Sections A and B. 22

3.5 Depletion region formed between coplanar contacts 24

3.6 Equipotential map for Section A, modification 6, plane I = 1. 26

3.7 Equipotential map for Section B, modification 6, plane I = 60. 27

3.8 Equipotential map for Section A, modification 6, plane K = 7. 28

3.9 Equipotential map for Section B, modification 6, plane K = 7. 29

3.10 Equipotential map for Section A, modification 9, plane I = 1. 31

3.11 Equipotential map for Section B, modification 9, plane I = 60. 32

3.12 Equipotential map for Section A, modification 9, plane K = 1. 33

3.13 Equipotential map for Section B, modification 9, plane K = 1. 34

3.14 Equipotential map for Section A, modification 9, plane K = 40. 35

3.15 Equipotential map for Section B, modification 9, plane K = 40. 36

3.16 Equipotential map for Section A, modification 10, plane I = 1. 37

3.17 Equipotential map for Section A, modification 11, plane I = 1. 38

3.18 Equipotential map for Section A, modification 12, plane I = 1. 39

5.19 Bias network for TPGD. 45

5.20 Count rate versus depletion voltage. 46

6.21 Equivalent circuit for a semiconductor detector 48

6.22 Simplified schematic of a charge preamplifier. 50
6.23 Output of the TRIUMF charge preamplifier. 50
6.24 Simplified schematic of voltage preamplifier. 51
6.25 Output of voltage sensitive preamplifier. 52
6.26 Schematic of the input of the Ortec 109A charge preamplifier. 53
6.27 The modified hybrid charge preamplifier with amplifier and drive circuitry. 54
6.28 Calibration of charge preamplifier/qVt system. 55
6.29 Noise in charge measuring system as a function of peak position. 56
6.30 Schematic of voltage sensitive amplifier system. 58
6.31 Response of voltage amplifier to test pulse. 59
6.32 Calibration of voltage sensitive amplifier. 59

7.33 Geometry for collection of ^{241}Am data. 62
7.34 Response of TPGD/amplifier to α-particle. 63
7.35 ^{241}Am α-particle spectra for an air separation of 27 mm. 64
7.36 ^{241}Am α-particle spectra for an air separation of 8.0 mm. 64
7.37 ^{241}Am α-particle spectra for a Si detector (in vacuum) 65
7.38 Signal charge collected as a function of α-particle energy. 67
7.39 Geometry for measuring Ruthenium electrons. 69
7.40 Response of voltage preamplifier to ^{106}Ru electrons 70
7.41 ^{106}Ru spectra from the TPGD 70
7.42 Geometry of M11 experiment. 72
7.43 Spectra of large scintillator (without proton absorber). 73
7.44 Histogram of TPGD for 292 MeV/c protons and pions. 74
7.45 Proton spectra of TPGD after STAR CUTs. 74
7.46 Spectra of large scintillator (with proton absorber). 75

7.47 Histogram of TPGD for 292 MeV/c pions. 75
7.48 Pion spectra of TPGD after STAR CUTs. 76
7.49 Calculated efficiency of TPGD to 292 MeV/c protons and pions. 77
7.50 Response of TPGD/amplifier to protons and pions. 79
7.51 Calibration of STAR histograms in terms of energy. 80

B.52 Coplanar geometry of Schottky drift electrode and ohmic output electrode. 92
B.53 Coplanar plates conformally mapped into parallel plates. 92
B.54 Capacitance of coplanar plates. 93

Chapter 1

Introduction

1.1 Particle Detectors and Detector Interactions

Various types of particle detectors are used in nuclear and particle physics ranging from gaseous wire chambers through superheated liquids to semiconductors and other solids. All detectors obey the same basic principles and each exhibit specific advantages over the other types. Every detector consists of a medium with which incident radiation interacts and a means of analysing the effect of these interactions. In the majority of detectors (wire chambers, spark chambers, Geiger tubes, and semiconductors), the interaction results in the production of mobile charge carriers which are measured electronically. Other detectors rely on the production of light during the interaction (scintillators, emulsions) and subsequent detection of this light.

The interaction of the incident particle with the detector medium results in a loss of energy by the particle. This energy exchange can be described by one or more models depending on the nature of the radiation and the medium. For heavy charged particles such as protons, alpha particles and fission fragments, the energy loss is described in terms of the stopping power, S, of the medium which is given by the Bethe-Bloch formula [1]:

$$S = \frac{-dE}{dx} = \frac{4\pi e^4 z^2}{m_0 v^2} NB \qquad (1.1)$$

where

$$B = Z\left[\ln\left\{\frac{2m_0v^2}{I\,(1-\beta^2)}\right\} - \beta^2\right] \tag{1.2}$$

and

$$\beta = v/c \tag{1.3}$$

Z = atomic number of stopping medium

v = incident particle velocity

ze = charge on incident particle

N = number density of atoms in medium

m_0 = electron rest mass

I = average ionization potential of medium.

The Bethe-Bloch formula describes a Coulombic interaction between the incident particle and the electrons, where the average energy lost to a given atomic electron is much smaller than the energy of the particle (non-catastrophic collisions).

If the incident particle is an electron, the interaction is also Coulombic, but can be catastrophic in that the incident electron can have its momentum and energy changed greatly by a single interaction. Furthermore, because of their small mass, electrons can lose energy through radiation as they decelerate (Bremsstrahlung). These two processes are taken together to give a stopping power formula for electrons where:

$$\frac{dE}{dx} = \left(\frac{dE}{dx}\right)_{Coulomb} + \left(\frac{dE}{dx}\right)_{Radiative} \tag{1.4}$$

The Coulombic stopping power is given by:

$$-\left(\frac{dE}{dx}\right)_{Coulomb} = \frac{2\pi e^4}{m_0v^2}NB \tag{1.5}$$

where

$$B = Z\left[\ln\left\{\frac{m_0 v^2 E}{2I^2(1-\beta^2)}\right\} - \ln 2\left(2\sqrt{1-\beta^2}\right) + \left(1-\beta^2\right) + \frac{1}{8}\left(\sqrt{1-\beta^2}\right)\right] \quad (1.6)$$

[2] and the radiative stopping power by:

$$-\left(\frac{dE}{dx}\right)_{Rad} = \frac{N E Z (Z+1) e^4 \alpha}{m_0^2 v^4}\left(4\ln\frac{2E}{m_0 c^2} - \frac{4}{3}\right) \quad (1.7)$$

[2] where $\alpha \approx 1/137$.

It should be noted that the radiative process is only significant for electron energies above $600/Z$ MeV.

The interaction of photons with the detector medium is described by three processes (Compton effect, photoelectric effect, and pair production) whose relative importance depends on both the photon energy and the detector material. A linear absorption coefficient can be associated with each process and the sum, μ, of these coefficients (σ, τ, κ) used to describe the attenuation of a beam of such photons as they pass through the medium:

$$\frac{dI}{I} = -\mu\, dx \;\rightarrow\; I = I_0 \exp^{-\mu x} \quad (1.8)$$

The Compton effect describes scattering of a photon by atomic electrons and has a linear absorption coefficient (lac) given by [1, pp. 675,685]:

$$\sigma = N Z \frac{8\pi}{3}\left(1 - 2\alpha + 5.2\alpha^2 - \ldots\right) \quad (1.9)$$

where N and Z are as before; r_0 is the classical (Bohr) electron radius and $\alpha = h\nu/m_0 c^2$ is the ratio of the incident photon energy to the energy of an electron (.511 MeV).

The photoelectric effect involves the absorption of a photon by an atom and the subsequent ejection of an electron. It is characterized by a lac:

$$\tau = {}_a\tau N \tag{1.10}$$

where ${}_a\tau$ is the atomic cross section per atom of the medium and varies loosely as $Z^4/(h\nu)^3$.

Pair production can occur in the medium if the incident photon energy is greater than 2 × .511 MeV. The pair production lac is given by:

$$\kappa = \kappa_{Pb} \frac{\rho}{\rho_{Pb}} \frac{A_{Pb}}{A} \left(\frac{Z}{Z_{Pb}}\right)^2 \tag{1.11}$$

where κ_{Pb} is the lac for lead

ρ is the mass density

A = atomic weight

and Z = atomic number.

More detailed analysis of τ, σ, and κ shows that the photoelectric effect dominates for low energy photons and pair production dominates for high energy photons.

Uncharged particles such as neutrons lose energy to the detector medium through collisions with the nuclei of the material. These collisions result in the excitation of the nuclei which can decay producing photons and charged particles which are detected as described above. The probability of interaction can again be described by a cross section which varies with neutron energy and the type of medium.

Of practical consideration in comparing various detector media are the variations of S, τ, σ, and κ with N, Z, A, ρ, and I. Accordingly semiconductor detectors have

much greater stopping powers than gas detectors (greater ρ). Better energy resolution is obtained in semiconductors than in gases because of their lower values of I (3-5 eV in semiconductors; 30 eV in gases), and speed is greater because of the differences in carrier mobilities and drift distances. Disadvantages of semiconductor detectors include their limited size, susceptibility to radiation damage, and lower sensitivity to gamma rays (smaller Z) than scintillators (but still better energy resolution).

The overhead in running a semiconductor is somewhat less than that required to run gas or liquid detectors. Little or no cooling is required in many cases and bias voltages can be lower by 1 or 2 orders of magnitude over gas detectors. Semiconductor detectors can easily be operated under vacuum.

Semiconductor detectors (including Si, Ge, GaAs, CdTe, and HgI_2) are important in particle physics mainly because they exhibit better energy resolution and greater (and variable) mass thicknesses than other types of detectors. Individually; Ge detectors are restricted to low temperature operation because of the small band gap of Ge; Si detectors are restricted by silicon's low atomic number and hence low efficiency to the photoelectric effect; while the compound semiconductors have been limited by their purity and crystal quality. At present it is not possible to obtain detector quality CdTe or HgI_2 in sizes greater than a few square centimetres, while developments in the electronics industry have brought us high quality GaAs in 2" diameter and larger wafers. GaAs is a particularly enticing material in that it exhibits electron mobilities at least 6 times higher (at 300K [3]) than any of the above semiconductors, has a greater (observed [4]) efficiency than CdTe or HgI_2 [5], and is much more radiation resistant than popular Si detectors [6]. Under ionizing radiation GaAs MESFETs have a lifetime of 10^7 to 10^8 rads (GaAs), and GaAs CCDs are expected to have lifetimes greatly in excess of 1 Mrad, while Si MOS devices have a lifetime of 10^3 to 10^4 rad (Si) (bipolar Si can survive 10^6 to 10^7 rad (Si)). GaAs and Si are equally susceptible

to displacement damage by neutron radiation where lifetimes extend up to fluxes of 10^{15} cm^{-2} to 10^{16} cm^{-2} for FETs, while transfer efficiencies in CCDs show significant decreases at doses of 10^{12} to 10^{13} cm^{-2}. [7,8]

GaAs has been investigated in the past [5,9,10,3] for its suitability for use in particle detection and although results were encouraging, lack of high quality substrate material limited overall device sizes (3mm $\times$ 3mm $\times$ 60 micron sensitive areas) and resulted in performances not significantly better than those observed in silicon and germanium based devices.

1.2 Signal Charge Production

Of the energy deposited in the detector, only a fraction can be collected as a signal charge at the output of the device. The incident energy is absorbed by the semiconductor through the promotion of electrons to the conduction band in the production of electron hole pairs (ehp's), and in the production of phonons. The energy used to produce phonons is lost as far as signal charge is concerned, and the number of ehp's produced either by pair production or electron promotion will also decay through recombination processes.

Each semiconductor has an associated (statistical) quantity, w, being the energy deposited in the material by ionizing radiation required to produce an ehp. In GaAs, w ranges from 4.2 eV to 5.7 eV, depending on the type of radiation, the type of detector, and the manner used to measure it (see Section B.2). According to a theory by Shockley [11], this energy can be written as,

$$w = E_i + rE_r + 2E_f \tag{1.12}$$

where

E_i is the energy to produce an ehp,

r is the average number of phonons produced along with the production of an ehp,
E_r is the average energy of these phonons (35 meV in GaAs), and
$E_f < E_i$ is the average energy carried away by an electron or hole.
This ehp production energy, w, is equivalent to the ionization energy, I, used in the Bethe-Bloch equation.

The ehp's are produced in a column along the track of the particle, with a density given by the stopping power, or in a sphere about the point of interaction of a photon. Initially this column looks like a conductive wire passing through the semiconductor, tending to negate any drift field set up in the detector by external biases. In a time characterized by the dielectric relaxation time of the semiconductor ($\tau_R = \rho\epsilon_s = 10$ ps for GaAs doped at $N_D = 1 \times 10^{14}$ cm^{-3}), the drift field begins to penetrate the charge column. This takes place through ambipolar diffusion [12,13,14]. During this period there is a probability, depending on the density of ehp's, that ehp's will recombine and be lost from the signal charge. The two main recombination processes within the column are radiative and Auger recombination (in this context Auger recombination involves the collision between two free electrons and a free hole, or two free holes and an electron, where the recombination energy is carried off the extra electron or hole [15]). As the drift field of the detector penetrates the column, electrons and holes become spatially separated and these two processes are replaced in importance by impurity trapping as a mode of signal charge loss.

The three recombination processes are characterized by time constants [15], which depend on the density of free carriers (ehp's) in the region of interest. Figure 1.1 [16] shows the variation as a function of excess carrier density for GaAs. For heavily ionizing particles such as alpha particles, Auger recombination is important immediately after the formation of the column. As recombination, diffusion, and drift decrease the carrier density, radiative recombination becomes important. The photons released by radiative

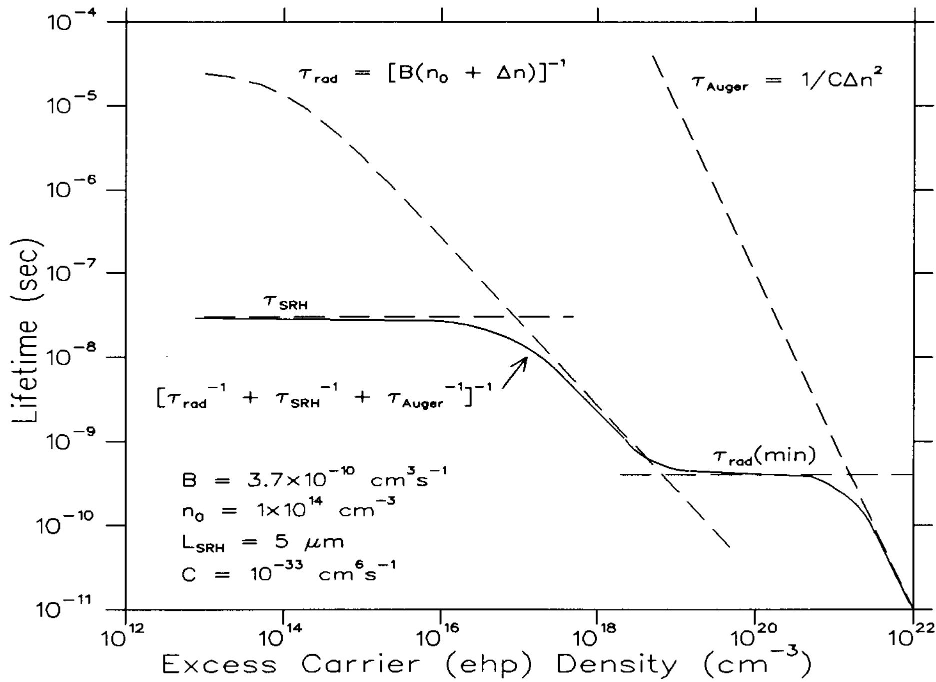

Figure 1.1: Time constants for different recombination modes. (After Hopkins and Srour [16]). Recombination at impurities is described as a Shockley-Read-Hall (SRH) process.

recombination in the column can be reabsorbed by the detector, but with a decreased probability as high carrier concentrations in the column result in a locally decreased band gap [17] and hence photons with an energy less than the equilibrium band gap. The effect of this recombination is discussed in Section 7.1. Once the drift field has penetrated the column and separation of electrons and holes occurs, signal charge loss is dominated by recombination at impurities. In addition trapping and later release by these impurities can distort signal pulses and lead to loss of energy resolution. The effect of impurity recombination and trapping is further discussed in Chapter 3.

Chapter 2

Proposal

With the establishment of a GaAs fabrication laboratory at TRIUMF in 1985, a decision was made to investigate the use of gallium arsenide as the interaction medium for detecting radiation. Three designs were considered; two using bulk grown wafers and one using an epitaxial grown layer on a bulk grown substrate. The use of bulk grown silicon (zone refined) in planar silicon detectors motivated the first two designs. However, it was soon decided that neither a bulk conduction nor diode design would work because of the poor quality of the bulk grown gallium arsenide. Traps in the material would make it unlikely that the radiation induced charge could be collected quickly and efficiently. Unlike the high resistivity of the silicon used in silicon detectors (which is due to the intrinsic nature of the material), the resistivity of semi-insulating (S.I.) GaAs is due to the presence of traps. Furthermore, it is very difficult if not impossible to make a good non-rectifying contact with S.I. GaAs because of the low carrier concentration in the GaAs.

The third design uses an epitaxial layer of high quality GaAs in which to detect radiation. Such devices have worked successfully in the past for large area detectors on conducting substrates [10]. For reasons discussed in Chapter 3 an epitaxial layer device on a S.I. substrate was proposed as follows:

> A test device is to be built on 20 μm epitaxial material (doped to $N_D = 10^{14}\text{cm}^{-3}$) grown on a S.I. GaAs substrate, to investigate the detection of ionizing radiation in such material. A drift field parallel to the

surface will be used to facilitate detection of minimum ionizing radiation (approximately 150 ehps per micron traversed) over a large area. Current technology and developed fabrication processes are to be used. The device will be characterized with various forms of radiation, and the physics of the interaction investigated.

Chapter 3

Device Design

3.1 Why Epitaxial GaAs?

An essential requirement of any particle detector is uniformity of the interaction medium over the active area of the device. Without homogeneity of the material it is impossible to establish uniform fields within the device with which to collect carriers produced by the radiation, and the detector is therefore inherently position sensitive, although not in a predictable manner. In Si and Ge, crystal growth technology has developed to the point where it is possible to produce ultra-pure single crystals of high enough resistivity that drift fields can be established over distances of hundreds of microns without breakdown occurring. Detectors with mass thicknesses large enough to allow the detection of minimum ionizing radiation by direct current sensing techniques can thus be fabricated.

Gallium arsenide crystals can not as yet be grown as purely and defect free as Si or Ge. As a result uniform fields can not be produced throughout macroscopic volumes and associated carrier trapping can result in loss of signal or space charge build-up. The enormity of the problem of traps in semi-insulating GaAs can be appreciated when one realizes that the high resistivity of the material is due to defects and to compensation by stray impurities in concentrations of 1×10^{15} cm^{-3} (10^{14} cm^{-3} net p- or n-type) [18], and not due to any intrinsic nature of the material. Unintentional compensation

results in net carrier densities around 10^8 to 10^9 cm^{-3} and resistivities of $> 10^7\Omega$-cm. Although this resistivity is close to the resistivity of a pure crystal, a pure crystal would exhibit a net doping density of 0 and an intrinsic carrier concentration of 1.8×10^6 cm^{-3} [19]. (A pure GaAs crystal with a net doping density of 1×10^{14} cm^{-3} would have a resistivity around 130 Ω-cm). In established electronic technologies on GaAs, this property can often be neglected, or at least circumvented, as the material used is doped such that its properties are extrinsic and dependent almost exclusively on the doping density. In particle detectors, where high resistivities are required, the "as grown" intrinsic properties of GaAs is of concern and limits the possibilities of the device. Furthermore, work done on bulk GaAs detectors [20] indicates that energy resolution is poorer than that obtained from epitaxial layers on semiconducting substrates. GaAs detectors on conducting or semiconducting substrates have been built as far back as the early 1970s [10], but because of their design have been limited in use to the detection of highly ionizing radiation. Also the epitaxial layers used for these detectors were fairly thick (60 to 200 μm) and are not commercially available. The investigation of ionizing particle detection in commercially available epitaxial layers on SI GaAs was proposed in light of these results and the following considerations.

3.2 Difficulties With GaAs

One of the primary reasons for the greater radiation hardness of GaAs devices over Si or Ge devices lies in the different fabrication methods employed. Radiation damage in Si devices is predominantly due to the breakdown of insulated gate structures which are not present in GaAs devices. Unfortunately the lack of a native oxide on GaAs also makes device isolation somewhat more difficult. On standard electronic devices on epitaxial GaAs, device isolation is achieved by removal of the epitaxial layer (down

to the SI substrate) between distinct active regions, or deactivation of the same areas by high energy ion bombardment, which destroys the local crystal structure. These technologies are developed only for thin epitaxial layers ($< 5\mu$m), and as such can not be applied directly to layers 20 μm thick. Device isolation using guard ring technology is proposed for the device to be examined. The use of this method has the additional benefit of helping to form the required fields in the device.

Because the detection element is to be built on an epitaxial layer and the expected signal will be small, the capacitance must be limited to achieve a reasonable signal to noise ratio. On a semiconducting (SC) substrate with a 20 μm epitaxial layer, this would limit the element size severely as the substrate would act like a metal plate producing a large capacitance at the output electrode on the surface as well as coupling separate outputs. On an SI substrate with an epitaxial layer in full depletion, there are no free carriers to form this backside "plate" and the capacitance is that of the electrodes patterned on the surface. By implementing a drift field parallel with the surface through the use of multiple drift electrodes (Schottky contacts) this capacitance can be minimized and the sensitive area per output electrode enlarged (Figure 3.2).

The major difference between the device designed here and earlier silicon drift chambers [21,22,23,24] is the lack of electrodes on both sides of the epitaxial layer. In my design, there is no means to contact the backside of the layer (and to do so would negate the advantage of using a SI substrate) at the substrate interface to set the potential there. However, for an n-type epitaxial layer on SI GaAs, a depletion region forms at this interface. The substrate acts as a p-type material probably due to the trapping of diffusion electrons (from the epitaxial layer) [25]. By itself this depletion region forms an electron potential minimum in the epitaxial layer (typically 3 to 4 μm inside the 1×10^{14} cm^{-3} material. See Section 3.5. Deyhimy et al. [25] suggest that the portion of the substrate near the interface acts as if it were doped $N_A = 1 \times 10^{16}$ cm^{-3}. This value

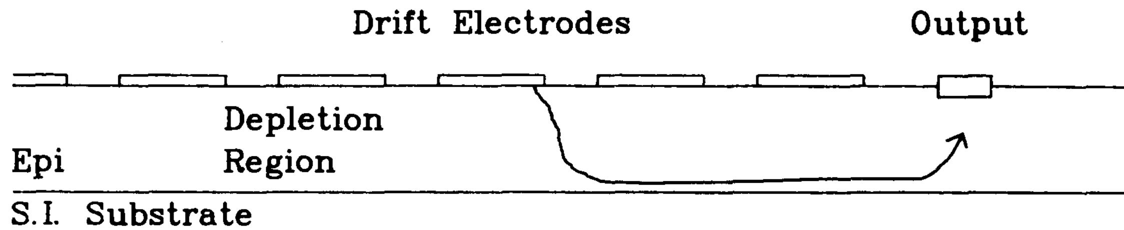

Figure 3.2: Charge collection by drift parallel to the surface. A voltage gradient is added to the voltage required to deplete the epitaxial layer by means of the drift electrodes. Electrons produced in the device will follow a path similar to that shown. Holes will travel in the opposite direction. Electrons are forced towards the substrate/epitaxial layer interface by the negative bias on the drift electrodes where they enter a potential trough. The drift field motions them along to the ohmic output. They are contained within the epitaxial layer by the built-in field of the epitaxial/substrate interface.

was used in modelling the device constructed). Normally the device will be operated such that the depletion region formed from the front side meets that formed from the interface, with the overlap producing a localized potential minimum near the meeting point. Holes produced by ionizing radiation passing through the depletion regions of the epitaxial layer will drift upwards to the Schottky electrodes where they will recombine with injected electrons, while radiation induced electrons will drift down to the potential minimum and along to the ohmic output electrode.

3.3 The TRIUMF Pixelized GaAs Detector (TPGD)

The TRIUMF Pixelized GaAs Detector (TPGD) (Figure 3.3) is a test device approximately 4 mm by 5 mm on a side. It has a (designed) radiation sensitive region of 2.88 mm by 4 mm by 20 μm deep, which is divided into 16 pixels. Each pixel has an Ohmic Output (O1 through O16) which is wire bonded to an IC package, or an in-package FET, by means of a bonding pad. The 8 pixels on each side of the device

share 6 Schottky drift electrodes (D1 through D6) having bonding pads at each end. Around the exterior of the device (outside the sensitive region) is a guard electrode structure consisting of a Guard Schottky (GS) electrode and a Guard Ohmic (GO) electrode. This structure isolates the 16 signal outputs from each other as well as from charge produced outside the sensitive region.

The ohmic electrodes make a non-rectifying contact between the signal outputs and the epitaxial GaAs with the aid of a highly doped N^+ layer and an alloyed metal deposition [26,27], while the drift electrodes perform two functions:

1. They are used to deplete the epitaxial layer by reverse biassing a Schottky barrier, and

2. They can provide a variable electric field (drift field) to drift electrons towards the Ohmic Outputs where they can be collected.

The difference in the electrical behaviour between the two types of electrodes (non-rectifying versus rectifying) results from the different fabrication procedures used to form them (see Chapter 4).

The drift electrodes are 20 μm across in the long direction of the device and 10 μm across at the ends of each pixel. They are routed in an **S**-shaped pattern to eliminate non-sensitive regions (regions that have not been depleted and therefore have no drift field to separate electrons from holes). With this design any radiation striking inside the Guard Schottky should be detected by electron drift to an Ohmic Output. The symmetry of the design introduces ambiguity as to determining which side of an Ohmic Output radiation strikes and hence position resolution is by pixelization only. Radiation incident directly on electrode D1 could result in a signal at 2,3, or 4 adjacent electrodes, but otherwise the output signal for a single event will be observed only at one output electrode (neglecting capacitive coupling which will be small).

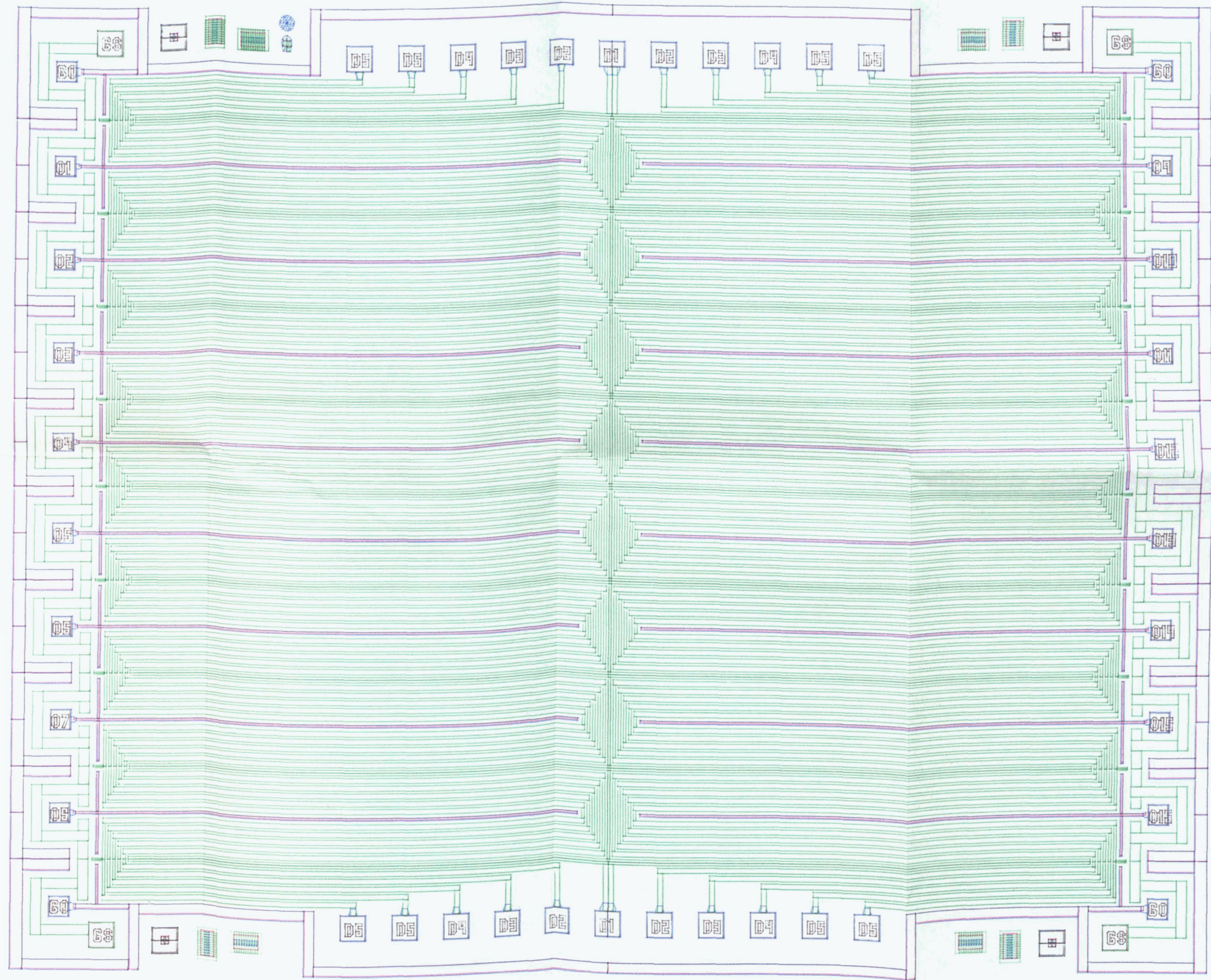

window: (-449, 6389, 390, 4489) scale: 167 lambda/cm cell: tpgd

L01 L02 L03 L04 L05 L06 L07 L08

Drift electrodes are separated by 10 μm in keeping with results by Deyhimy [25] indicating that the separation-to-epi-depth ratio be less than 1 to eliminate interelectrode potential traps, and to ensure as uniform a surface covering as possible. Drift of electrons towards the Ohmic Outputs is done by grading the voltages of D1 - D6. The drift field induced will be stepped near the surface (see results of modelling in Section 3.5), and must be kept less than the breakdown field. Because the depletion field appears between the Ohmic Output and D6 in addition to the drift field, the separation here is 15 μm. The Ohmic Output strip is 10 μm in width to minimize its capacitance.

When operated as a detector, the drift electrodes should completely deplete the epitaxial layer, except directly under the Ohmic Outputs. The region that has not been depleted will be insensitive to radiation as there is no field to separate electrons from holes.

The use of relaxed design rules (smallest feature = 6μm) eases the alignment requirements during fabrication.

3.4 Device Considerations

Of interest in the construction of a semiconductor detector are estimates of signal size, depletion volume, detector capacitance, operating voltage and noise. Calculations of these quantities are given in Appendix B, and what follows is a discussion of the expected detector response for minimum ionizing radiation incident on the detector.

The energy required to create an electron-hole pair in GaAs is approximately 4.2 eV [10,28]. For minimum ionizing radiation depositing 1.2 MeV cm^2g^{-1}, ehps are produced at a rate of approximately 150 per micron compared with 80 per micron in Si. Thus in a 20 μm epitaxial layer a minimum signal of 3000 ehps can be expected. On a SC

substrate, fully depleted regions will have a depletion capacitance of $\epsilon/20\mu m = 580$ pF/cm^2, and hence a (static) signal voltage of $0.83\mu V\ cm^2$ will be measured directly. To get a signal of at least 1 mV a diode structure no larger than 83000 μm^2 can be used. In terms of radiation detectors this is a very small area. With a SI substrate and a fully depleted epitaxial layer, the epitaxial layer thickness does not play a part in the detector capacitance. As the holes and electrons of the signal charge are separated across the Schottky drift electrodes and the ohmic output electrode, the capacitance to be considered is that formed by the coplanar electrodes. If the drift electrodes are approximated by a semi-infinite sheet separated from the Ohmic Output contact by 15 μm the calculated capacitance is 2.64 pF/cm of output length, or 0.61 pF for the TPGD. This is an effective capacitance of 85 pF/cm^2 of surface area.

The detection of this signal will depend on the amount of noise produced in the system. This noise can be expected to comprise Johnson noise, dark currents, generation currents, and surface currents. The Johnson noise will depend on the ohmic contact resistance and the capacitance of the external circuit and will vary as kT/C_{ext}, where C_{ext} is the combined capacitance of the detector and amplifier input [29]. The equivalent noise charge will be, $N_J \approx 400\, C_{ext}^{\frac{1}{2}}$ (C_{ext} in pF) at room temperature, or 315 elemental charges per output of the TPGD.

Dark current will be negligible compared with generation current [11], which is expected to result in the production of 2×10^{11} ehps per cm^2 of detector area per second, or 2.8×10^9 ehps/s in the active volume of a single pixel[29]. In the time taken to collect the signal charge (≈ 2 ns) this amounts to a noise of only 6 electrons. Combining these noise sources results in an expected signal to noise of $3000/320 \approx 9$ for minimum ionizing radiation. This is the expected noise at the output of the TPGD to which the noise of the amplifying system must be added.

Surface leakage currents are very much dependent on device geometry and fabrication procedures and can not be predicted a priori.

3.5 Computer Modelling

3.5.1 The RELAX3D Program

In addition to analytic calculations to determine capacitances and signal size, the potential field was modelled using the program RELAX3D [30] to see whether or not collection by drift over the region of the pixel is possible. Simulations with and without a p-type layer at the epitaxial/substrate interface indicate that this layer is necessary to contain signal charge within the epitaxial layer. Charge produced within the substrate is not expected to contribute to the signal because of the high impurity concentration there. The modelling presented here incorporates the doping levels determined during operation of the TPGD rather than those specified in the original design in order to understand the performance of the actual device.

RELAX3D is used to solve Poisson type equations on either a 1,2, or 3 dimensional grid using a relaxation technique. Boundary conditions are entered through a FORTRAN subroutine and can be one of three types: Dirichlet, Neumann, or dielectric. In essence a Dirichlet boundary is one in which the potential is fixed, while at a Neumann boundary, equipotential lines are perpendicular to the boundary. The interface between two dielectrics can be modelled by the use of a bound surface and bulk charge, and is done automatically by the program only for a Laplacian problem. In modelling the TPGD only Dirichlet and Neumann boundary conditions are used. The top and the bottom of the cubic regions modelled were held at fixed potentials (except between the topside electrodes where Neumann conditions are used), while the sides are symmetry

planes and Neumann conditions apply. The large relative permittivity of gallium arsenide (12.9) justifies the use of Neumann conditions between the electrodes on the top (air) surface.

The RELAX3D program was designed to be application independent and frugal on both CPU time and memory requirements. As such it has a fixed (for any given problem) grid spacing and a maximum number of grid points of 500,000. This poses a problem when dealing with the variable charge density of an epitaxial/substrate problem. In solving a Poisson equation, the grid points should be separated by a length on the order of a Debye length:

$$L_D \equiv \sqrt{\frac{\epsilon_s kT}{q^2 N_D}} \tag{3.13}$$

which for the epitaxial layer ($N_D \simeq 1 \times 10^{14}$) is 0.4 micron. If this grid separation is used for the entire epitaxial/substrate problem, the surface area that can be modelled must be fewer than 400 points. To circumvent this problem, the modelling was approached in two parts. Firstly, Laplace's equation was solved on a sparse grid for the full wafer thickness, and then, using these results, Poisson's equation was solved on the top 40 μm of the wafer. This scheme makes use of the principle of superposition whereby the total potential is thought of consisting of two parts.

$$\varphi_{total} = \varphi_{Laplace} + \varphi_{Depletion} \tag{3.14}$$

Poisson's equation for φ_{total} can then be split into two equations as follows:

$$\nabla^2 \varphi_{total} = \nabla^2 \varphi_{Laplace} + \nabla^2 \varphi_{Depletion} = -\frac{\rho}{\epsilon} \tag{3.15}$$

where one takes

$$\nabla^2 \varphi_{Laplace} = 0 \tag{3.16}$$

$$\nabla^2 \varphi_{Depletion} = -\frac{\rho}{\epsilon} \tag{3.17}$$

In modelling the TPGD, $\varphi_{Laplace}$ is found for the total thickness of the wafer and used to set the backside potential for the higher resolution Poisson problem. The depletion voltage for a given charge density is calculated and added to the surface electrodes and Poisson's equation solved.

3.5.2 The Modelled Sections

Two regions of the TPGD were modelled (Figure 3.4) to determine the drift field towards the Ohmic Output contact. The regions (Section A and Section B) model either end of the Ohmic Output contact's **T** structure in the sensitive region of the detector. As both extend down the length of the **T** to the extent that the problems become 2-dimensional, the solutions can be checked against each other.

Both modelled sections are orthorhombic in shape. Neither section includes all 6 drift electrodes, as not all are required to see what is happening. The total size of Section A is $48 \times 45 \times 100$ points, while that of section B is $65 \times 75 \times 100$.

The Laplace Problem

In the Laplace problem the modelled sections are on grids of $2\mu \times 2\mu \times 6\mu$. The backside of the wafer (K = 100; z = 600 μ) is fixed at a potential equal to the Ohmic Output contact, as this is what the package in which the TPGD was mounted was held at. The drift electrodes are fixed to give an average electric field of 0.75 kV/cm towards the Ohmic Output contact. No depletion voltage is added between the Ohmic Output contact and the drift electrodes.

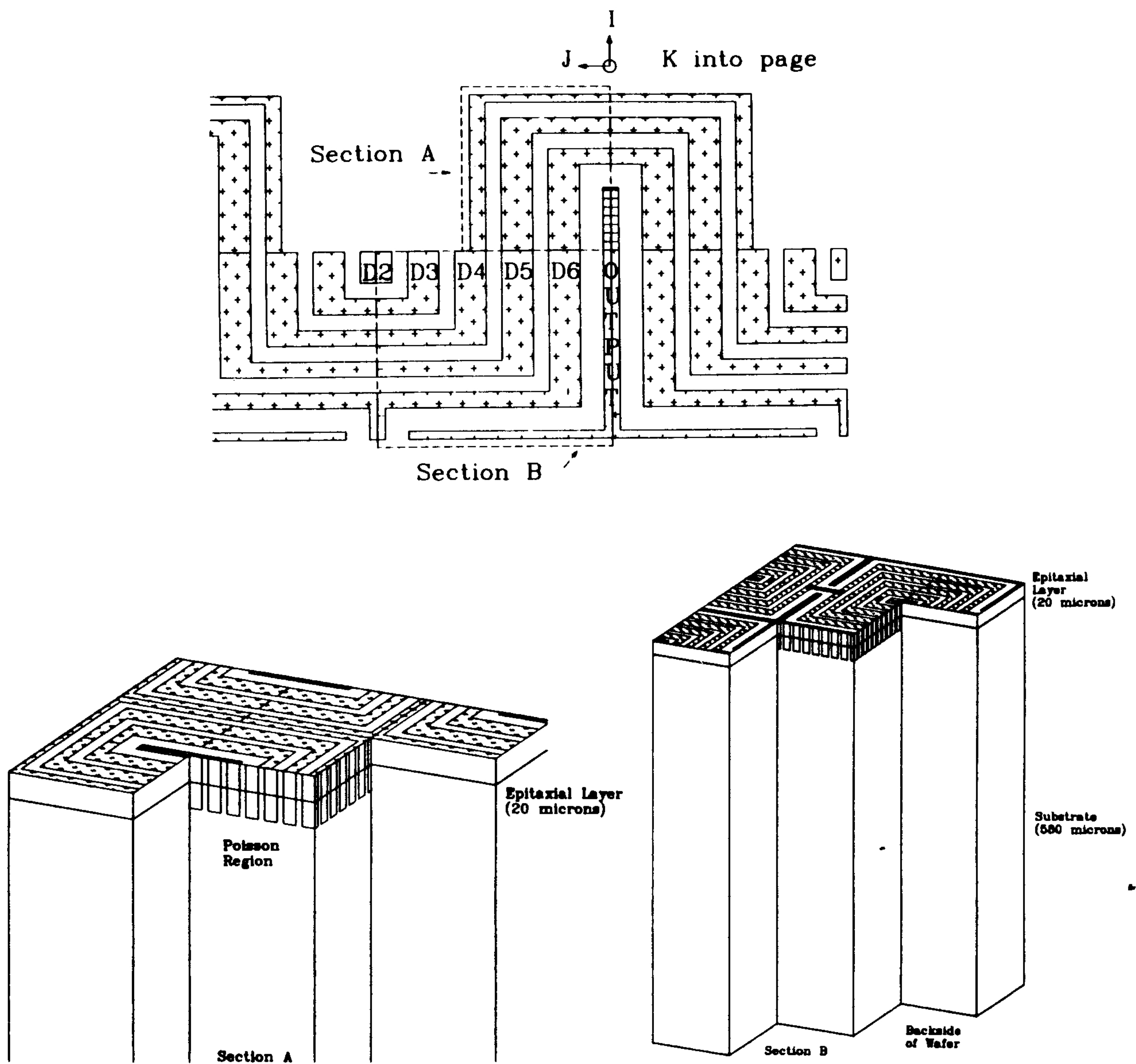

Figure 3.4: Modelled Sections A and B.
Top: A plan view of the modelled sections showing how they can be butted together to check solutions. Both ends of the Ohmic Output contact are modelled.
Bottom left: A 3-D view of the Section A showing how the symmetry planes of the sides of the modelled region would be reflected outside the region. The modelled region for Poisson's equation is shown.
Bottom right: A similar 3-D view of Section B showing the full substrate thickness to scale.

The Poisson Problem

In the Poisson problem the modelled sections are on grids of $2\mu \times 2\mu \times 0.4\mu$. The backside of the cube (K = 100; z = 40 μ) is fixed at the potential determined by the Laplace problem for that depth in the substrate. The drift electrodes are fixed to give an average electric field of 0.75 kV/cm towards the Ohmic Output contact and a fixed depletion voltage is added to the Ohmic Output contact and the backside of the cube. The use of a fixed depletion voltage (the same over the entire area of the problems) is a simplification which leads to some problems as described below.

3.5.3 Predetermined, Fixed Charge Distributions

The choice of an electrostatic, non-variable charge density program for modelling is a compromise between accuracy of solutions and complexity of the programming. In modelling the TPGD, an n-doped epitaxial layer is assumed to exist on top of an undoped substrate. The substrate is assumed to act p-type when forming an interface with the epitaxial layer [27,25] in some simulations, and inert in others. As the charge density is fixed for the duration of a simulation, the definition of the charge distribution is critical to the solution. For all simulations, the entire epitaxial layer was taken as having been fully depleted and thus has a charge density equal to the donor density. Complete depletion of the epitaxial layer will occur under the drift electrodes (Figure 3.5), but not under the Ohmic Output electrode. This is where the compromise is made. By taking the region under the Ohmic Output contact as having been fully depleted, one is saying that a very large voltage is being applied between the Ohmic Output contact and the drift electrodes: much greater than that needed to deplete the epitaxial layer thickness. Since this large voltage is not present in the various simulations, the solutions show potential minima for electrons under the Ohmic Output

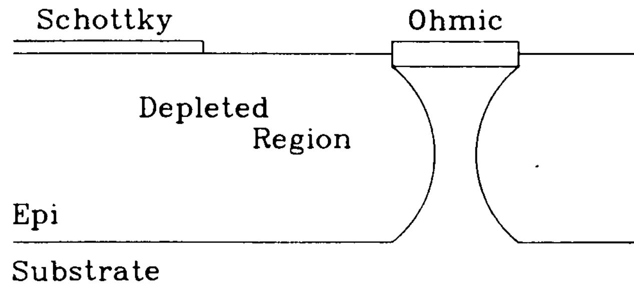

Figure 3.5: Depletion region formed between coplanar contacts. The depletion region reaches down and away from the Schottky Contact, forming a bowl shaped space charge region. To extend under the ohmic contact would require an extremely large depletion voltage.

contact because of the uncompensated (by applied voltage) positive charge in that region. In the semiconductor, these minima can not exist as the separation of electrons from their parent donor atoms would introduce an electric field which would not be compensated for by another mechanism in this region. As the purpose of the modelling was to show the presence or absence of drift towards the ohmic contact in the epitaxial layer, this oversight was neglected.

3.5.4 Results

Modelling of the two end regions of the TPGD was done for various different boundary conditions as discussed below. Both Section A and B are discussed for the operating conditions used, while only Section A is discussed when considering variations from these nominal conditions.

Laplace Problem

The boundary conditions used for the Laplace problem are given in Table 3.1. The labelling of electrodes is the same as that done on the actual device (Figure 3.3). As the

Electrode	Backside	Ohmic	D6	D5	D4	D3[1]	D2[1]
Voltage (V)	26	26	20	16	12	8	4

Table 3.1: Boundary conditions for Laplace problem.

sides of the box regions modelled are symmetry planes of the device, Neumann boundary conditions are applied there. The equipotential maps produced by the relaxation for Section A are shown in Figures 3.6 and 3.8 and for Section B in Figures 3.7 and 3.9. Figures 3.6 and 3.7 show a dipole like field near the surface electrodes which will drift electrodes towards the output electrode. The plane I = 7 (z = 42 μm) shown in Figures 3.8 and 3.9 are used for the backside of the Poisson problem. Both show drift towards the **T** in this plane.

Poisson Problem

The boundary conditions used for the various Poisson problems are given in Table 3.2, and the results of the simulation for the TPGD assuming a depletion voltage of 11V (modification 9) is shown in Figures 3.10 through 3.15. Figures 3.10 and 3.11 show that electrons produced in the epitaxial layer ($k \leq 51$) will be contained in the layer and drifted towards the output electrode (at $K = 1$, $J \leq 3$). For reference Figures 3.12 and 3.13 are equipotential maps of the surface showing where the cut planes were taken relative to the electrode structures. The potential minimum wells shown below the output electrode will not exist in the TPGD as discussed in Section 3.5.3. The path taken by the electrons will be first downward to the potential trough, and then along to the output electrode region. This potential trough resides between 2 and 5.6 μm away from the substrate; being closer to the substrate as one moves away from the output electrode. Figures 3.14 and 3.15 show drift towards the output electrode at a depth of 16 μm ($K = 40$).

[1]Section B only.

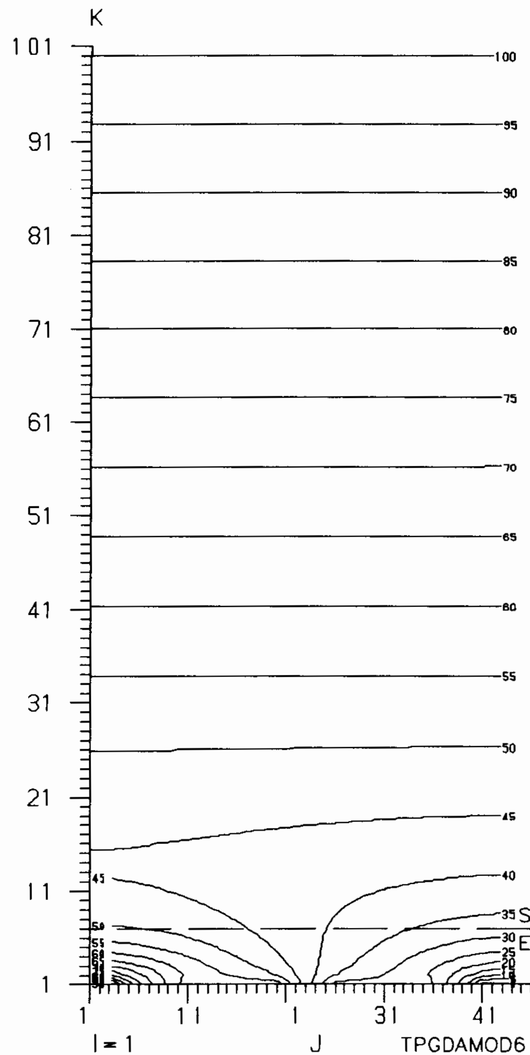

Figure 3.6: Equipotential map for Section A, modification 6, plane I = 1. Output electrode is at K = 1, J $\leq$ 3. Drift electrodes are at 10 $<$ J $\leq$ 20 (D6); 25 $<$ J $\leq$ 35 (D5); 40 $<$ J (D4). The dashed line shows the position of the epitaxial/substrate interface. Numbering on the equipotentials is in terms of percent of the voltage range for the simulation.

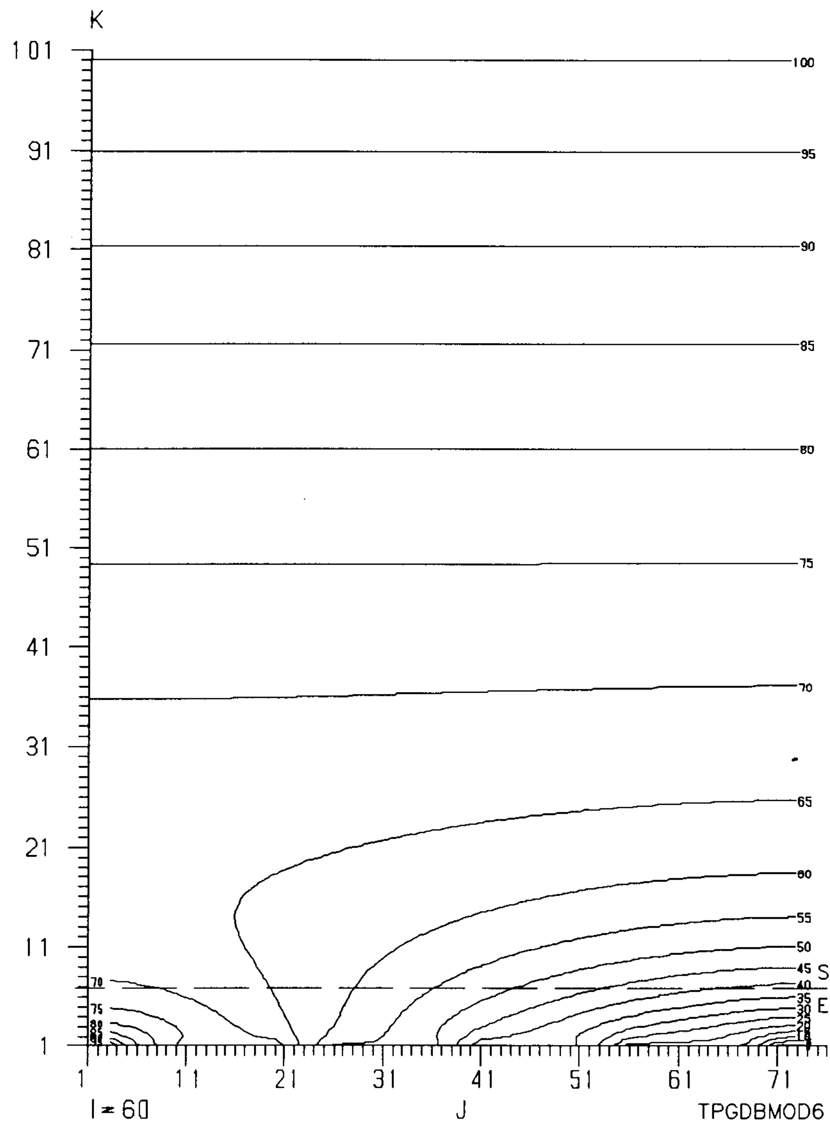

Figure 3.7: Equipotential map for Section B modification 6, plane I = 60. Output electrode is at K = 1, J$\leq$ 3. Drift electrodes are at $10 < J \leq 20$ (D6); $25 < J \leq 35$ (D5); $40 < J$ (D4). The dashed line shows the position of the epitaxial/substrate interface.

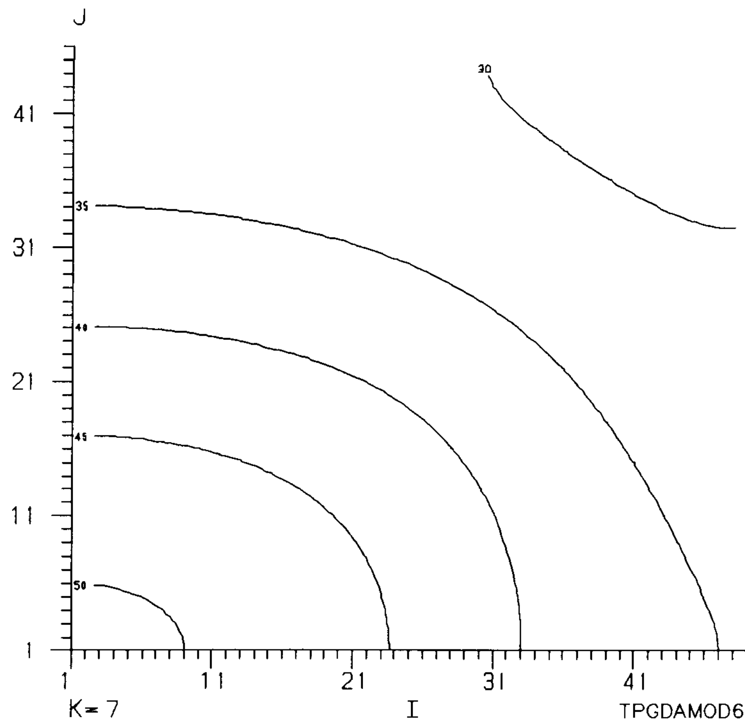

Figure 3.8: Equipotential map for Section A, modification 6, plane K = 7. This plane is used as the backside for the Poisson equation.

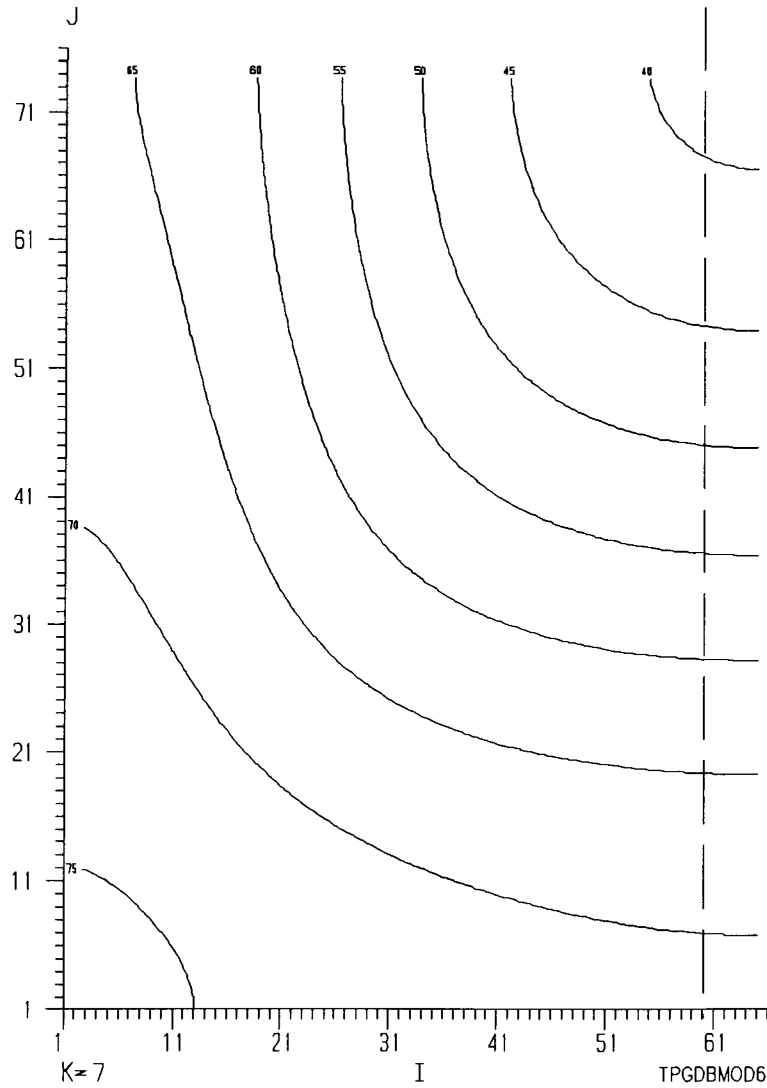

Figure 3.9: Equipotential map for Section B, modification 6, plane K = 7. The dashed line at I = 60 shows where the cut was taken for Figure 3.7.

Modification #	Epitaxial Doping $\times 10^{14}$ cm^{-3}	Interface Doping $\times 10^{14}$ cm^{-3}	Electrode Voltage						
			Backside Laplace +	Ohmic V	D6 V	D5 V	D4 V	D3[2] V	D2[2] V
9	0.67	7.58	11 V	37	20	16	12	8	4
10	0.67	7.58	15 V	41	20	16	12	8	4
11	0.40	0	15 V	41	20	16	12	8	4
12	1.0	8.51	19 V	45	20	16	12	8	4

Table 3.2: Boundary conditions for Poisson problems.

Variations in the electric field due to changes in doping densities and depletion voltages are shown in Figures 3.16 through 3.18. As the depletion voltage is increased for fixed doping densities to produce an over-depletion (modification 10, Figure 3.16) the potential trough is pushed towards and into the substrate. If the interface charge produced by the epitaxial/substrate interface does not exist, electrons will be lost to the substrate as shown in Figure 3.17. If the epitaxial layer doping is increased (modification 12, Figure 3.18) the potential trough is pushed towards the substrate and becomes narrower.

All modelling was done without the inclusion of the signal charge produced by ionizing radiation and the results are static solutions. The signal charge will initially short out the electric field because of the high density of free charge produced along the particles path. As this signal charge diffuses, the field will reform and drift will occur. The speed at, and the extent to which this field reforms will depend on the signal charge density.

[2]Section B only.

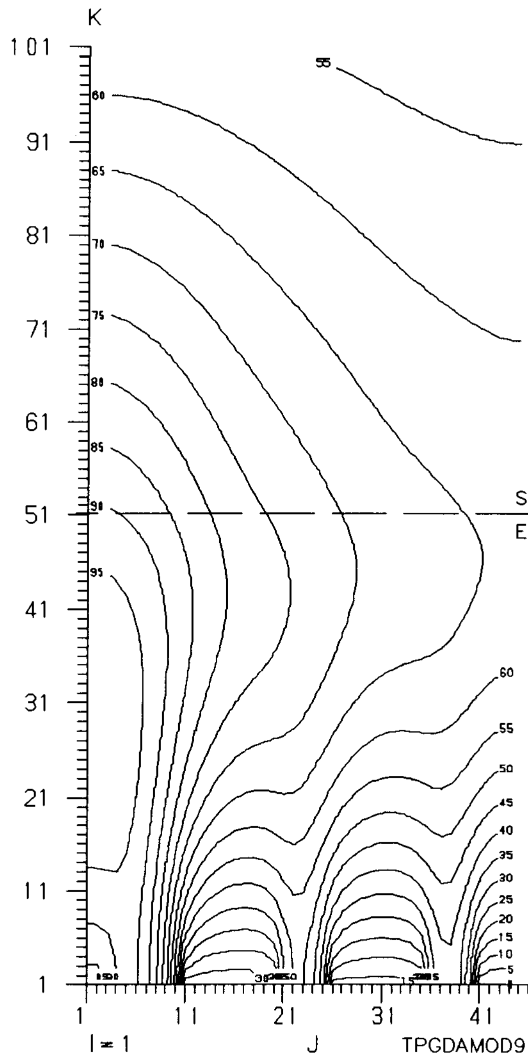

Figure 3.10: Equipotential map for Section A, modification 9, plane I = 1. A potential trough exists just above the substrate.

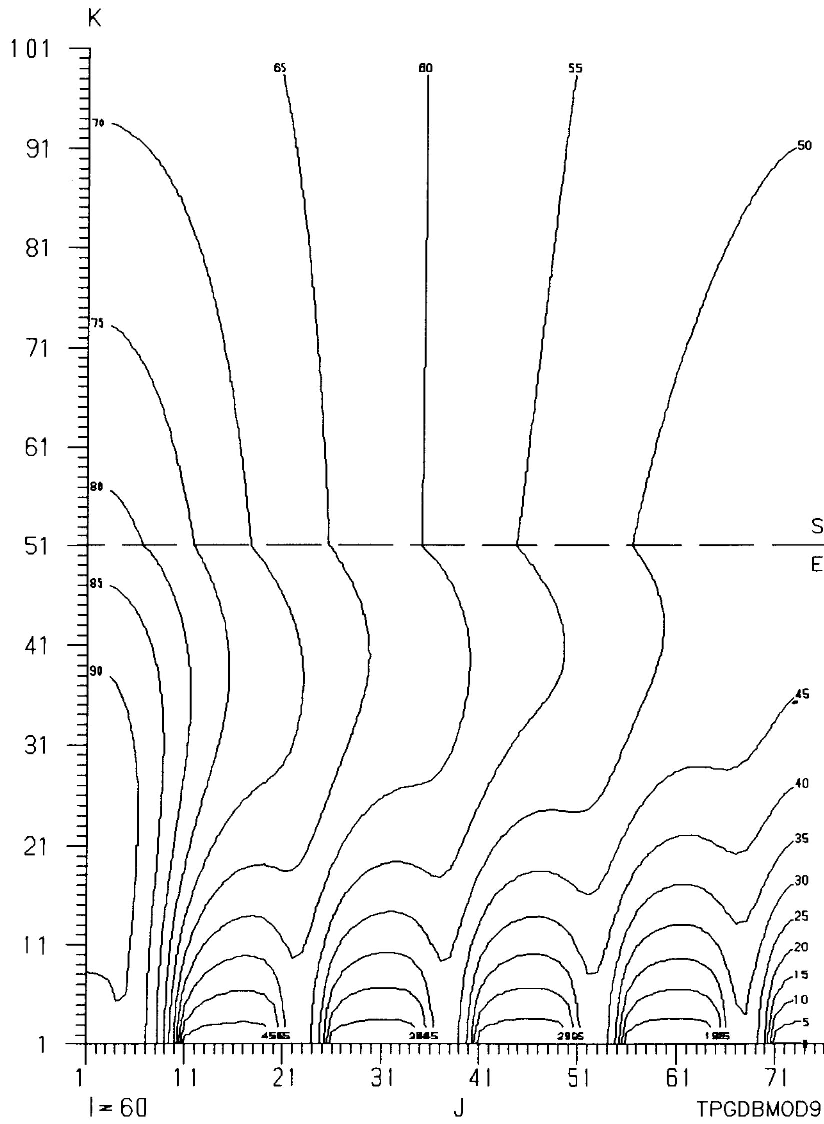

Figure 3.11: Equipotential map for Section B, modification 9, plane I = 60.

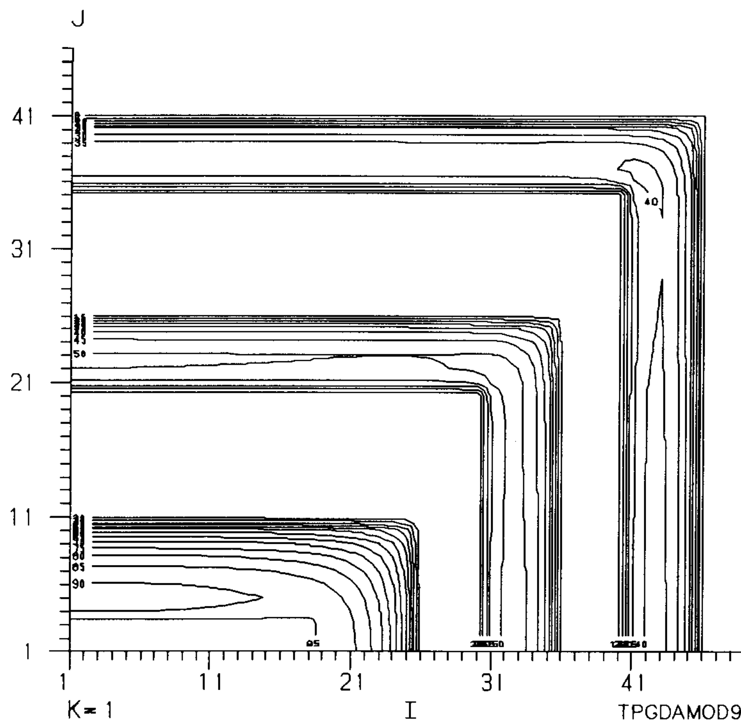

Figure 3.12: Equipotential map for Section A, modification 9, plane K = 1. The positions of the output and drift electrodes are visible as equipotential surfaces. The cut plane for Figure 3.10 is at I = 1.

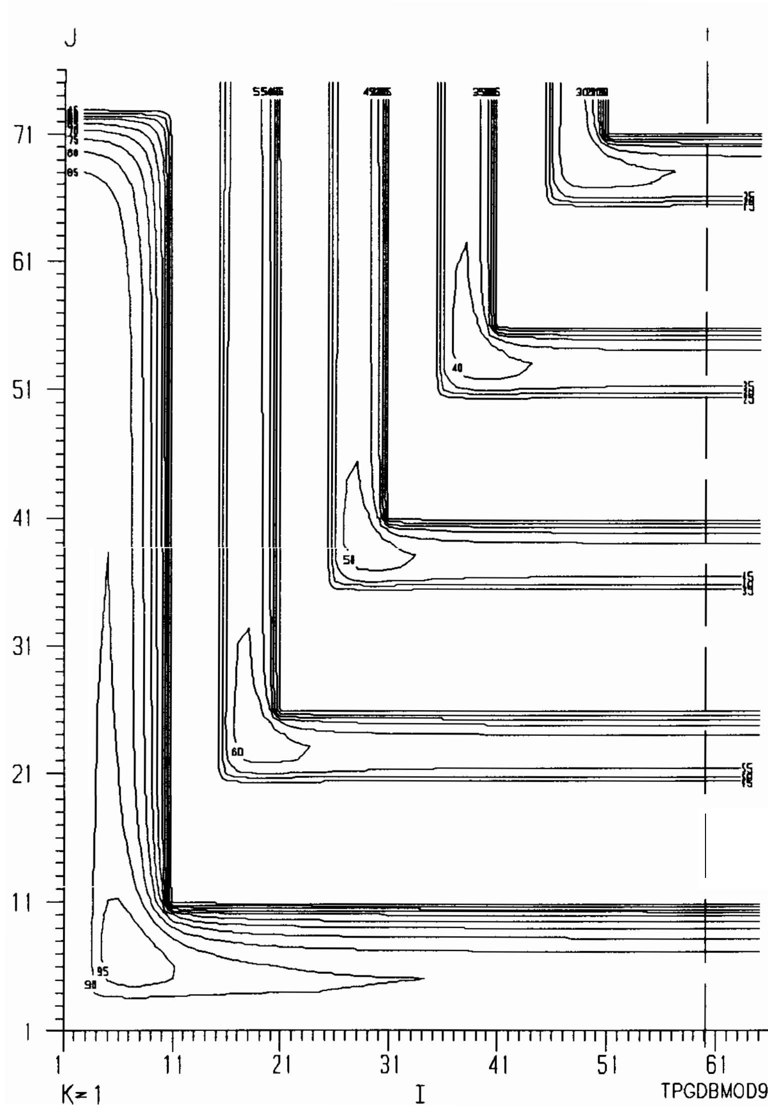

Figure 3.13: Equipotential map for Section B, modification 9, plane K = 1. The vertical dashed line indicates the cut plane used for Figure 3.11.

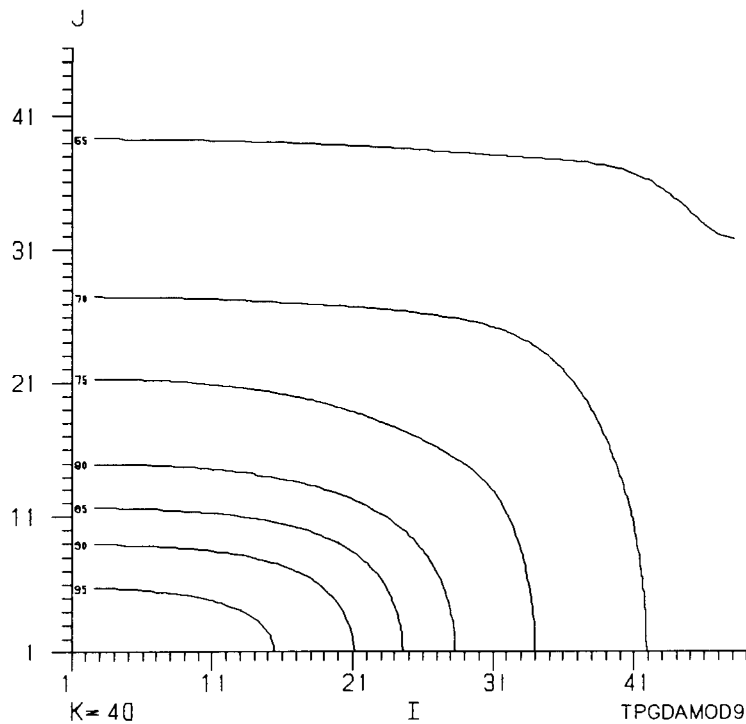

Figure 3.14: Equipotential map for Section A, modification 9, plane K = 40. This is approximately the median plane of the potential trough.

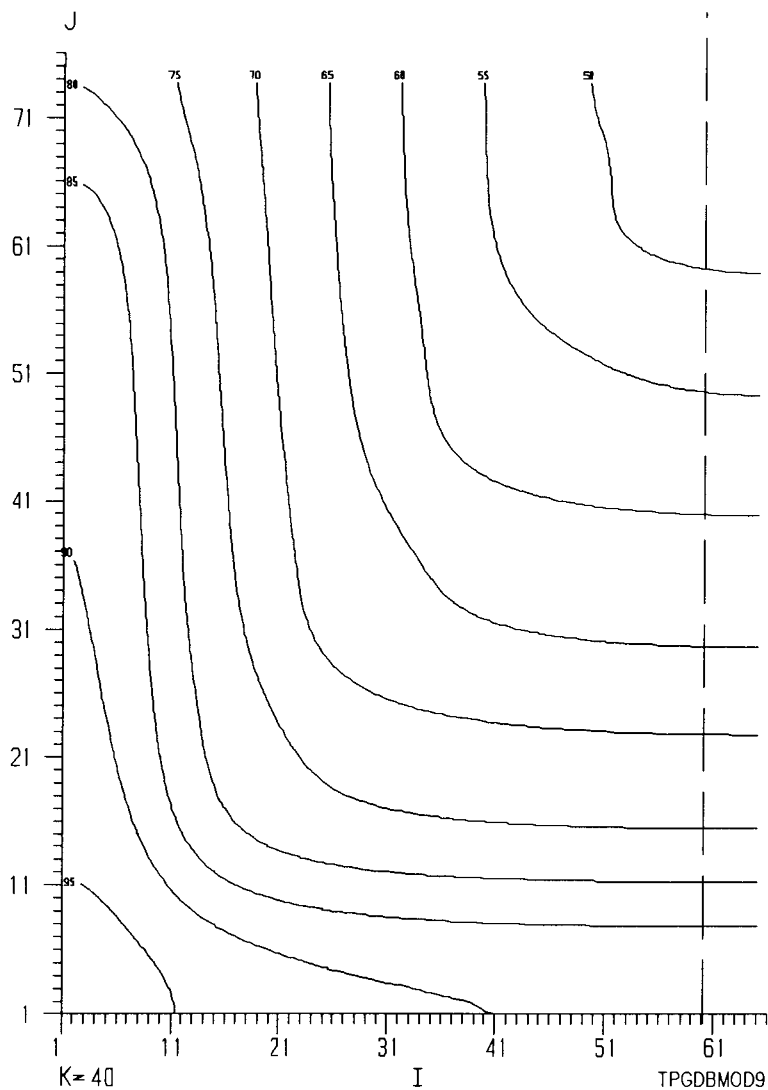

Figure 3.15: Equipotential map for Section B, modification 9, plane K = 40. Drift towards the ohmic electrode in the potential trough.

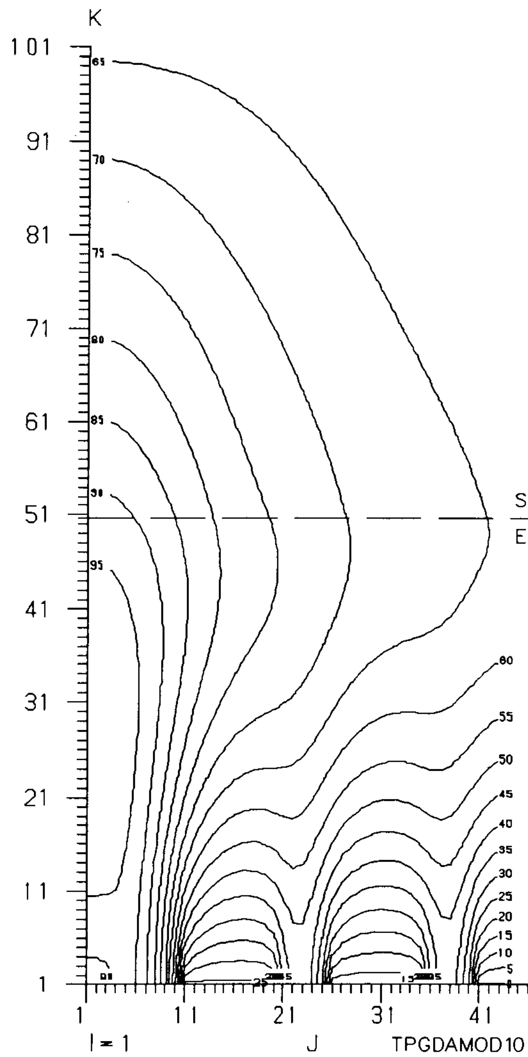

Figure 3.16: Equipotential map for Section A, modification 10, plane I = 1. A 4 V over-depletion has been added to the boundary conditions used in modification 9.

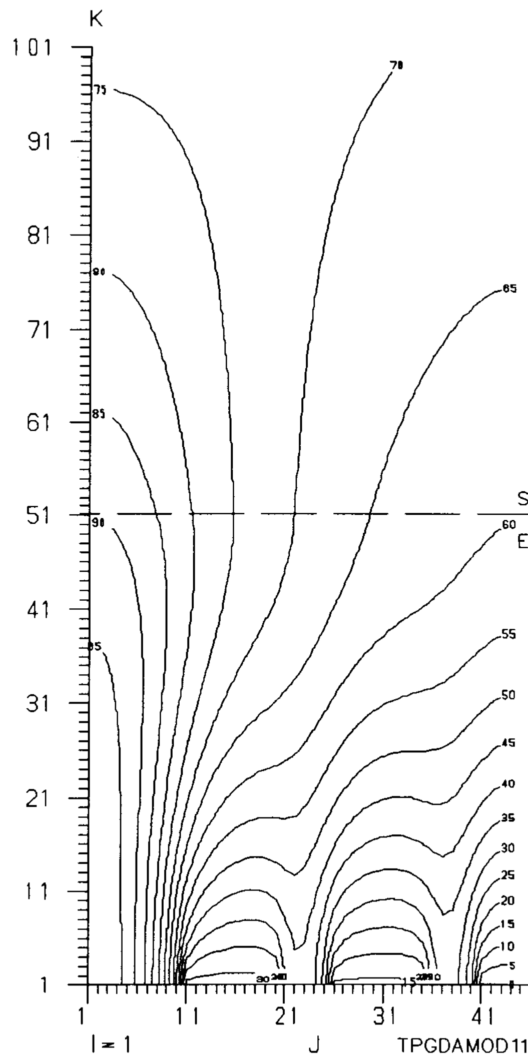

Figure 3.17: Equipotential map for Section A, modification 11, plane I = 1. The substrate is taken as being inert and not producing a depletion region into the epitaxial layer. Electrons can not be contained in the epitaxial layer with this structure.

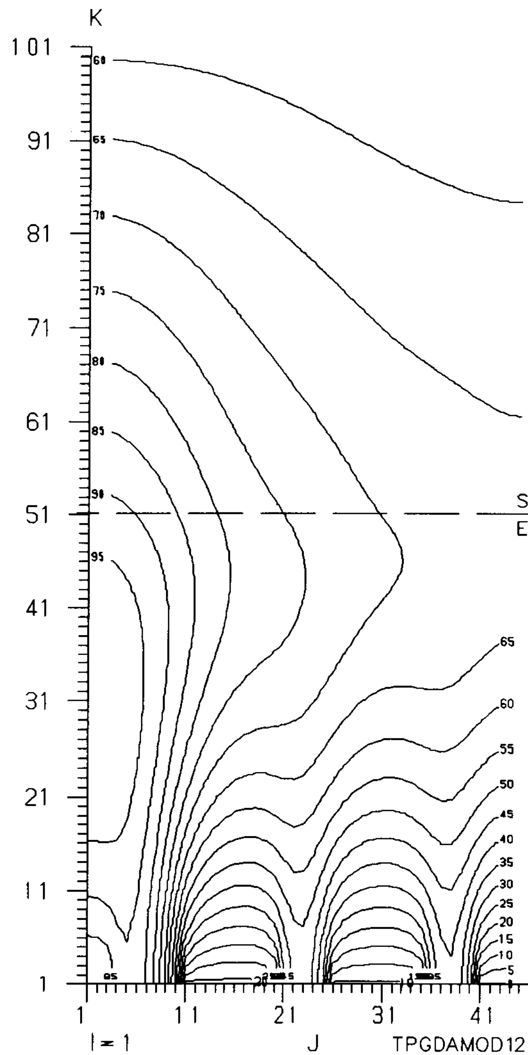

Figure 3.18: Equipotential map for Section A, modification 12, plane I = 1. An epitaxial doping density of $N_d = 1 \times 10^{14}$ cm^{-3} results in a narrower potential trough.

Chapter 4

Fabrication of the TRIUMF Pixelized GaAs Detector (TPGD)

The microelectronics fabrication lab at TRIUMF was set up primarily to allow in-house fabrication of gallium arsenide charge coupled devices (CCDs). These devices are required in fast transient digitizers for a particle physics experiment at Brookhaven National Laboratory. The lab is dedicated to GaAs device fabrication, and comprises the basic equipment required to produce devices on predoped material. Most of the fabrication procedures have been standardized, and will not be described in detail here (see [31]). The central piece of equipment is a Karl Süss aligner (MJB 55), which is used to align a patterning mask and semiconductor wafer to within 1 μm. The TPGD masks used in the aligner were manufactured at Precision Photomask[1], from a database layed out at TRIUMF using the CAD program KIC (developed at the University of California in Berkeley).

The fabrication process can be conveniently divided into routines which are completed, with slight modifications, for each mask layer. These routines are outlined in Appendix A. One of the design criteria for the TPGD was to keep the fabrication process as simple as possible and as a result only 3, or sometimes 4, masks are required. These are:

1. Layer L01 - N^+ etch

2. Layer L03 - Ohmic metallization

[1] St. Laurent, Quebec

3. Layer L05 - Schottky metallization

4. Layer L06 - Vias

The via mask allows the optional coating of the device with a protective polyimide film.

The names of the masks are indicative of what they are used for. A test plug was included on the masks to facilitate monitoring the fabrication, and evaluating the material. In all cases patterning on the wafer is done using a positive photoresist, exposed with the mask in hard contact with the wafer. Overall, the masks were satisfactory, except for the following problems:

1. The tracks outside of the bonding pads make bonding difficult and can lead to arcing from the bond wires down to these tracks.

2. The metallization on the majority of the bond pads is ohmic metal only and bonding to them is not always possible. The Schottky metallization mask should include all bonding pads. This problem was remedied by using the via mask to deposit an overcoating of gold on the pads.

3. The length of the Schottky metallization traces (≈ 4 cm) makes liftoff difficult to do cleanly.

The complete fabrication process required between 12 and 20 hours in the lab per run, depending on the difficulties encountered. Four runs were started, and three completed. In all runs a 1/4 wafer was used, and in each case varying amounts of breakage occurred. Although breakage is not uncommon in GaAs processing, the large amount of breakage experienced with this wafer compared with other wafers processed by the author, indicates that this wafer had been stressed during growth.

At the completion of processing, the wafer is scribed and broken into individual die. A visual and electrical inspection is completed before the die are wire bonded into packages.

Chapter 5

Electrical Measurements

During and immediately after fabrication, the TPGD and the test plug were used to evaluate the progress and results of the fabrication procedure. Once bonded, simple electrical tests were performed on the TPGD and dual-in-line-package (DIP) to verify bond connections and to observe any aging. A biassing circuit was built and bias leakage currents measured.

5.1 Fabrication Stage

The N^+ etch depth was measured using an Alpha-Step 200 Profiler and checked both on the TPGD and test plug electrically. The high conductivity of the N^+ layer ($N_D = 1 \times 10^{18}$ cm^{-3}; $\rho = 1.3$ mΩ-cm) makes this test straight forward. The test plug included on the mask set contains structures for measuring diode and ohmic contact characteristics, and metallization resistances. The I-V characteristics between ohmic contacts on the plug are linear to $\pm$20V, giving a calculated resistivity of the 'active' epitaxial layer of 400 kΩ-cm. This is equivalent to an average electron concentration throughout the epitaxial layer of $\leq 5 \times 10^9$ cm^{-3}. This measurement depends on the quality of the ohmic contact which could not be evaluated at this carrier density with the available equipment; however, it is apparent that the doping density was not as specified for the device design. A measurement of the depletion capacitance showed no change in capacitance for reverse biases up to 30 V on a Schottky diode, also indicating no measurable carrier densities in the epitaxial layer. A further calculation of depletion

Electrode to Electrode	Maximum allowable leakage Current (μA)
D_i to D_j $(i, j = 1, 6)$	1 μA at ± 10 V
D6 to GO	0.5 μA at -18 V
D6 to Ohmic Output	0.5 μA at -25 V
D6 to GS	0.5 μA at ± 10 V
GS to GO	0.5 μA at ± 20 V
GS to Ohmic Output	0.2 μA at -20 V

Table 5.3: Leakage current criteria for the TPGD.

depth indicates that the epitaxial layer would be depleted by the built-in potential on a p-n junction for electron densities $< 1 \times 10^{13}$ cm^{-3} (Table B.6). It was concluded from these tests that the active doping concentration was less than 1×10^{13} cm^{-3}.

The capacitance between the drift electrode, D6, and the nearby Ohmic Output contact was measured using an Alessi probing station and a Hewlett Packard 4275A LCR meter as 490 ± 10 fF, in good agreement with calculated values. Leakage currents (essentially due to surface leakage at this doping density) were measured between drift electrodes, and between drift electrodes and ohmic electrodes (reverse biassed). Diode structures could be biassed in the forward dirction to voltages between 8 V and 15 V before conduction was observed. No true diode conduction was observed. Leakage currents (node to node) for devices to be bonded up were less than those given in Table 5.3. Each 1/4 wafer processed contained between 11 and 16 devices (before breakage), of which 2 to 4 had acceptable leakage currents.

5.2 Post-Bonding Stage

Acceptable TPGD die were bonded into a 48 pin DIP. Two of the five die bonded up included in-package FETs on some of the 16 output pads. A second FET, or resistor was included in these packages to reset those outputs (see Figure 6.24). After bonding,

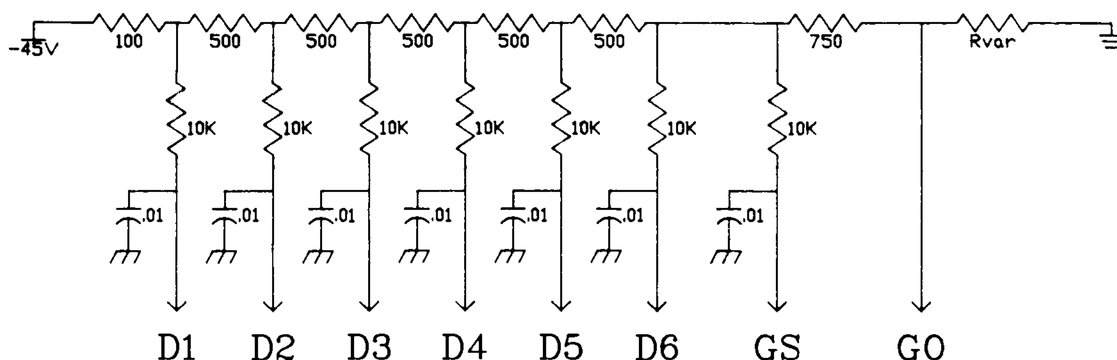

Figure 5.19: Bias network for TPGD. The 500 Ω and 750 Ω resistors are potentiometers, and were adjusted along with R_{var} to set drift fields and depletion voltages.

the package was checked for shorts and open circuits, and rebonded as necessary. The capacitance between D6 and the nearby Ohmic Output contact was measured as 3.9 pF for those packages without internal FETs.

A resistor network (Figure 5.19) was built to provide a variable voltage gradient across the six drift electrodes, Ohmic Outputs, Guard Schottky and Guard Ohmic electrodes.

5.3 TPGD Operating Conditions

The TPGD was designed to operate with a depletion voltage of 19 V and a drift field of 1.3 kV/cm. This assumes a built-in depletion from the backside of the epitaxial layer of 3.4 μm (V_{bi} = 0.8 V). The results of the C-V tests to -30 V depletion implied that that large a depletion voltage was not required. To check this further, count rates were taken for depletion voltages of 0 to -25 V using a fixed alpha source. Figure 5.20 shows a leveling off in count rate at -10 V indicating a saturation in the sensitive area of the TPGD. This was the only evidence obtained indicating that the epitaxial layer was not depleted either to start with, or by the built-in voltage of the metallization and substrate interfaces. From this data, the voltage required to deplete the 20 μm was taken as 11 V.

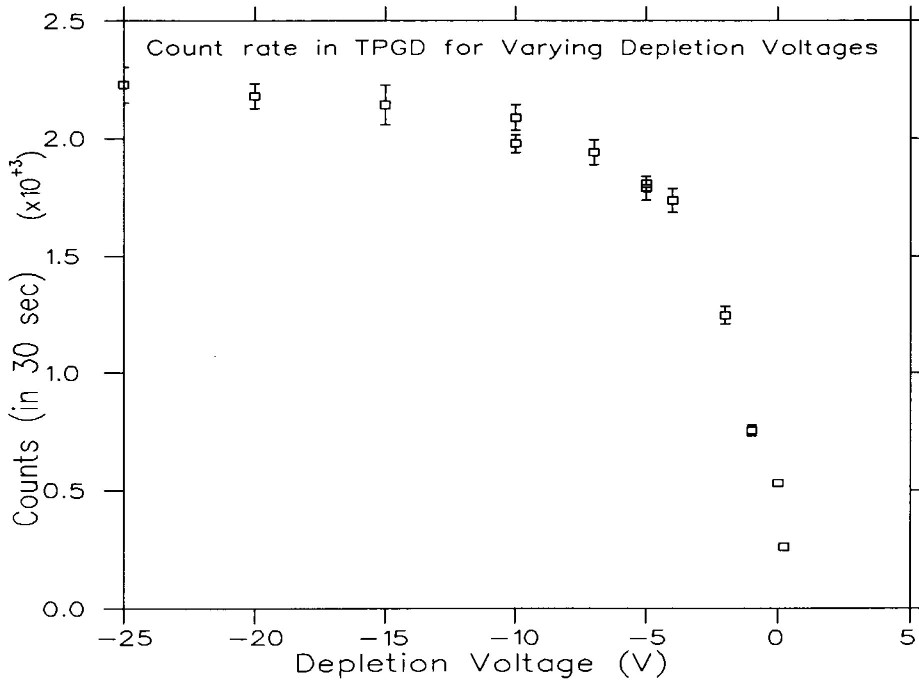

Figure 5.20: Count rate versus depletion voltage.

This indicates a net doping density in the epitaxial layer of $N_D = 6.7 \times 10^{13}$ cm^{-3}, which was used in the updated computer modelling presented in Section 3.5. For depletion voltages above 25 V, the drift field had to be reduced to prevent arcing between the bonding pad of D1 and the nearby GO trace.

For alpha particle measurements, the TPGD was run with and without drift fields in an attempt to determine the origin of the low energy peaks (see Section 7.1 and Figures 7.35 and 7.36). No difference in spectra was observed for the different operating conditions. The results presented in Section 7.1 were collected with a depletion voltage of 17 V and an inter-drift electrode voltage of 4 V.

For the in-beam experiment (Section 7.3), the depletion voltage was set at 15 V and the drift voltages at 5 V between neighbouring drift electrodes. An attempt to increase this to 20 V depletion resulted in breakdown between the D1 bond pad and

the GO at fields of < 10 kV/cm.

Chapter 6

Amplifiers and Data Collection

Three different amplifier configurations were used on the output of the TPGD. Two of these were charge preamplifiers and the third a source follower coupled voltage amplifier. The choice of amplifier is governed by the impedance of the TPGD, the expected input signal and the required output signal. The TPGD can be modelled (simply) as a capacitance in parallel with a large resistance (Figure 6.21) on whose output nodes a charge Q_{sig} is placed by a current source i_{sig}. This current source simulates the current pulse arising from an incident ionizing particle, while the resistor models other forms of generation, recombination and leakage currents within the TPGD.

The measured capacitance of the TPGD is 0.5 pF, while the expected charge varies from 3000 electrons for minimum ionizing radiation to over 1 million electrons for an ^{241}Am α-particle. This represents a peak voltage across the TPGD varying from 1 mV to 340 mV neglecting leakage currents. The amplifier must be able to sense this charge

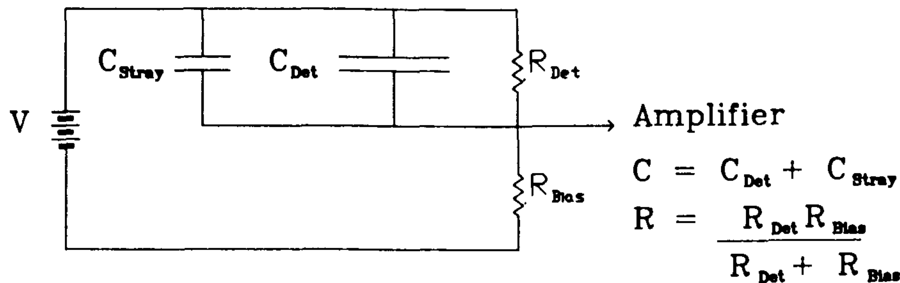

Figure 6.21: Equivalent circuit for a semiconductor detector

and output a voltage readable by data acquisition systems (typically 0 – 1 V into 50 Ω). This transformation is one of impedance matching with slight amplification, and was approached in two ways. One; by transferring the charge onto a low impedance input (charge preamplifier), and two; by sensing the voltage across C_d using a high impedance voltage preamplifier.

Figure 6.22 is a simplified schematic for a charge sensitive preamplifier connected to the TPGD. A signal charge Q_{sig} results in a small voltage change, Δv, at the input of the preamplifier which upsets the equilibrium value of the input. The inverting amplifier attempts to drive the input back to its equilibrium value by slewing its output 180° out of phase with the input. In doing so a charge equal to $-Q_{sig}$ is passed through the feedback capacitor, cancelling the input signal. If the amplifier slew rate is sufficiently fast with respect to leakage currents both on the detector and in the amplifier, this results in a voltage $\Delta V = Q_{sig}/C_f$ across the feedback capacitor which appears at the output. If the amplifier has an open loop gain of A, the input of the preamplifier has a capacitive reactance of $1/\omega AC_f$, which can be quite low for the rise time of the signal charge ($\sim$ 10 ns). The voltage at the output of the preamp will remain fixed until the charge is drained off the feedback capacitor, or a new signal charge is produced across C_d. In the charge preamplifiers used, this is done with a resistor, R_f, in parallel with C_f, allowing the charge to drain off with a time constant, RC_f, which is much longer than both the the collection time of the detector and the rise time of the amplifier. Figure 6.23 shows the output of the charge preamplifier made at TRIUMF.

Figure 6.24 is a simplified schematic of the voltage sensitive preamplifier used with the TPGD. The signal charge, Q_{sig} is divided across the detector capacitance and the gate capacitance of the Field Effect Transistor (FET) (typically 0.3 pF for the Dexcel DXL 2502A FET used), resulting in a signal voltage of $Q_{sig}/(C_d + C_{FET}) = V_{sig}$. The FET is configured as a source follower and the input impedance of $\sim 1/\omega C_{FET}$ is

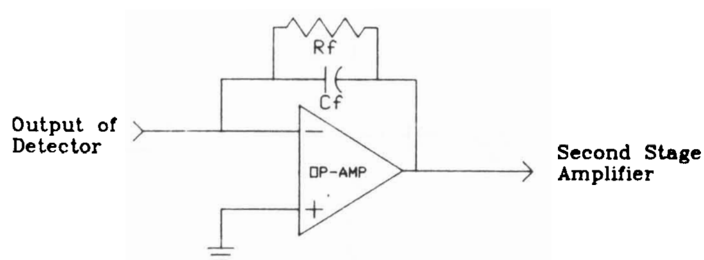

Figure 6.22: Simplified schematic of a charge preamplifier.

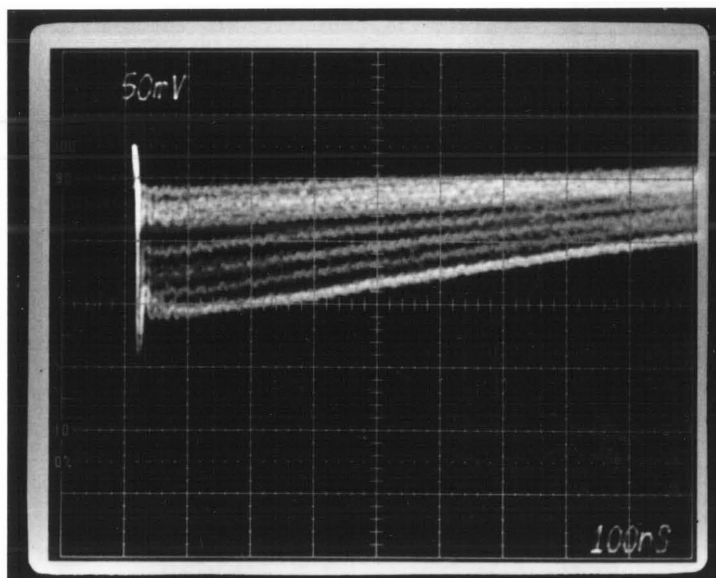

Figure 6.23: Output of the TRIUMF charge preamplifier. Scale is 50 mV/div; 100 ns/div. The source is ^{241}Am.

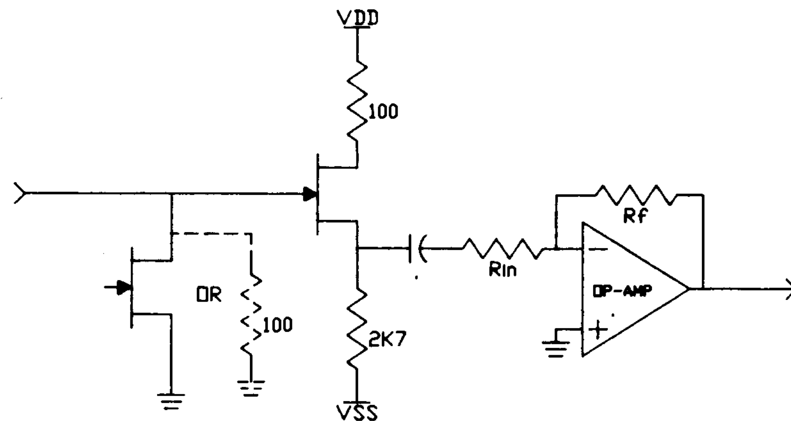

Figure 6.24: Simplified schematic of voltage preamplifier.

transformed into a much lower output impedance (equal to $1/g_m \sim 25\Omega$, where g_m is the transconductance of the FET) capable of driving the lower input impedance of a voltage amplifier. Unlike the charge preamplifier, the output voltage of the source follower (essentially V_{sig}) is not simply related to the charge as the capacitance of the FET varies with its operating conditions. Unless the detector capacitance dominates the FET capacitance, precise measurements of Q_{sig} are difficult to make. However, because of the higher input impedance of the source follower, this voltage preamplifier configuration is more sensitive to smaller values of Q_{sig}. Figure 6.25 shows the output of the voltage amplifier made at TRIUMF. The tail of the pulse depends on the charge leakage off the gate of the FET, and is done through a resistor to ground.

6.1 Charge Preamplifier Circuits

One commercially available charge preamplifier (an Ortec 109A) was used to look at pulses resulting from incident alpha particles. This amplifier has an ac-coupled input, which is referenced on the detector side of the coupling capacitor (see Figure 6.26) to

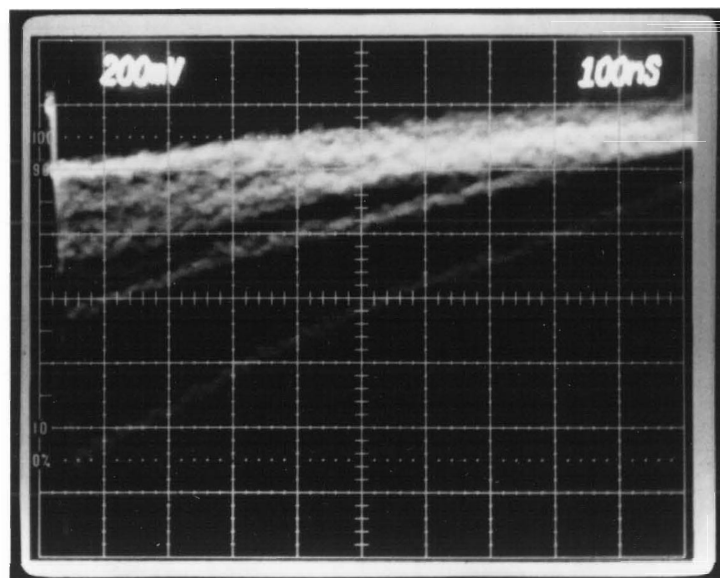

Figure 6.25: Output of voltage sensitive preamplifier. Scale is 200 mV/div; 100 ns/div. Source is ^{106}Ru.

ground through 1 MΩ. The preamplifier is designed to be extremely stable, but because of the low capacitance of the TPGD and the ac-coupling, rates as low as 20 cps caused unacceptable offsets in the output of the amplifier. A plausible explanation for this can be argued by considering that the signal charge results in a relatively large change in depletion voltage ($\sim$ 11 V) of the TPGD, which upsets the system. This offset can be reduced by decreasing the size of the referencing resistor (R_{ref}), which leads to other problems within the preamplifier. To solve this problem, a dc-coupled preamplifier (Figure 6.27) was built. This preamplifier is a modified version of a TRIUMF design[1]. The front end FET (Q1) is a GaAs FET used to minimize input capacitance and increase the slew rate of the preamplifier. The operational amplifier (NE5539) is a high speed amplifier with a gain of -10 which drives a 50Ω line through Q7. Transistor Q8

[1]TRIUMF DRW #B 1740

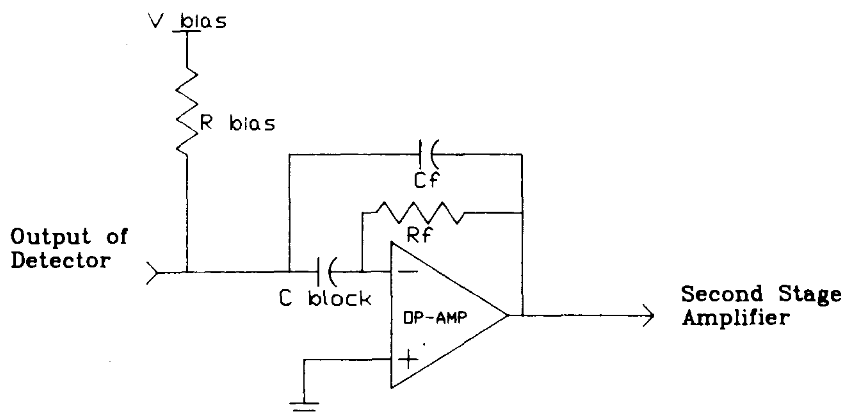

Figure 6.26: Schematic of the input of the Ortec 109A charge preamplifier.

is used to impedance match the amplifier circuitry to the q-input of a LeCroy model 3001 qVt multi-channel analyser.

The amplifier/analyser system was characterized by coupling a negative going, 60 ns wide pulse (repetition rate = 500 Hz) through a 10.2 pF capacitor, to the gate of Q1. The amplitude of the pulse was varied using a Hewlett Packard attenuator. The pulse generator is back terminated in 50Ω to minimize pulse shape distortion. Peak positions and FWHM were measured on the qVt, and used to calibrate the system. The number of elementary charges injected into the amplifier is given by:

$$Q_{cal} = VC_{coupling} \times 6.25 \times 10^{18} \tag{6.18}$$

while the noise of the system can be calculated from the FWHM of a peak in the qVt spectrum by:

$$ENC = \frac{m \times FWHM}{2.354} \qquad [11] \tag{6.19}$$

where

ENC is the Equivalent Noise Charge,

$FWHM$ is in channels,

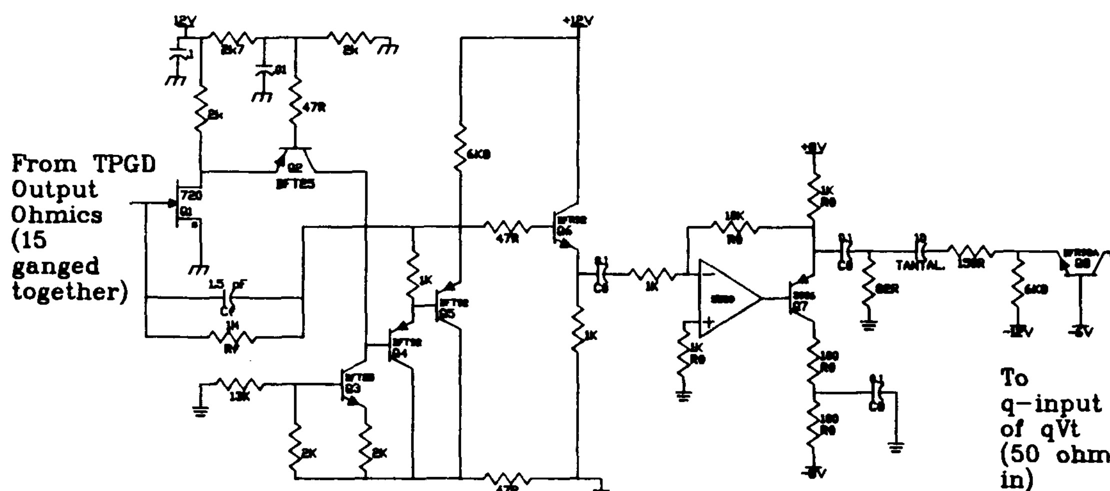

Figure 6.27: The modified hybrid charge preamplifier with amplifier and drive circuitry.

m is the calibration slope of the system in electrons per channel,

and the 2.354 factor accounts for the Gaussian shape of the pulse.

A calibration curve is given in Figure 6.28 and the dependence of noise on signal size is given in Figure 6.29. In all cases the noise is similar in size to the expected signal from minimum ionizing radiation. In terms of the incident particle energy, the system calibration is given by:

$$E = Qw = \left(1.22 \times 10^3 \times Chan.No. - 8.0 \times 10^4\right) \times w \qquad (6.20)$$

where

Q is the charge deposited (collected)

and w is the energy required to produce an electron-hole pair (ehp) in GaAs.

The energy resolution is given in the same manner:

FWHM (in energy) = FWHM (in ENC) $\times w$

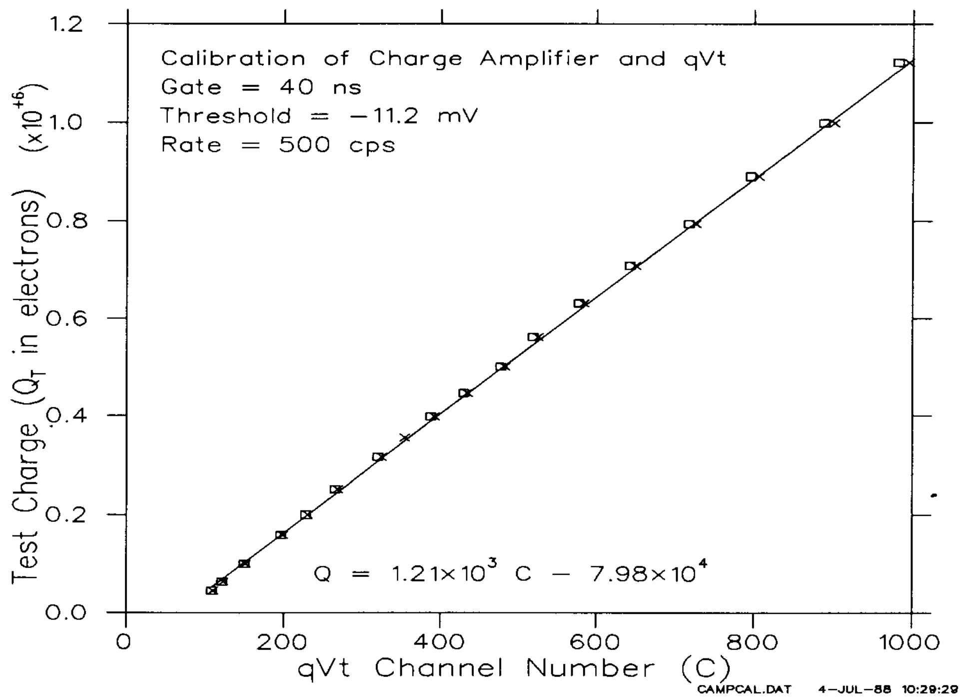

Figure 6.28: Calibration of charge preamplifier/qVt system.

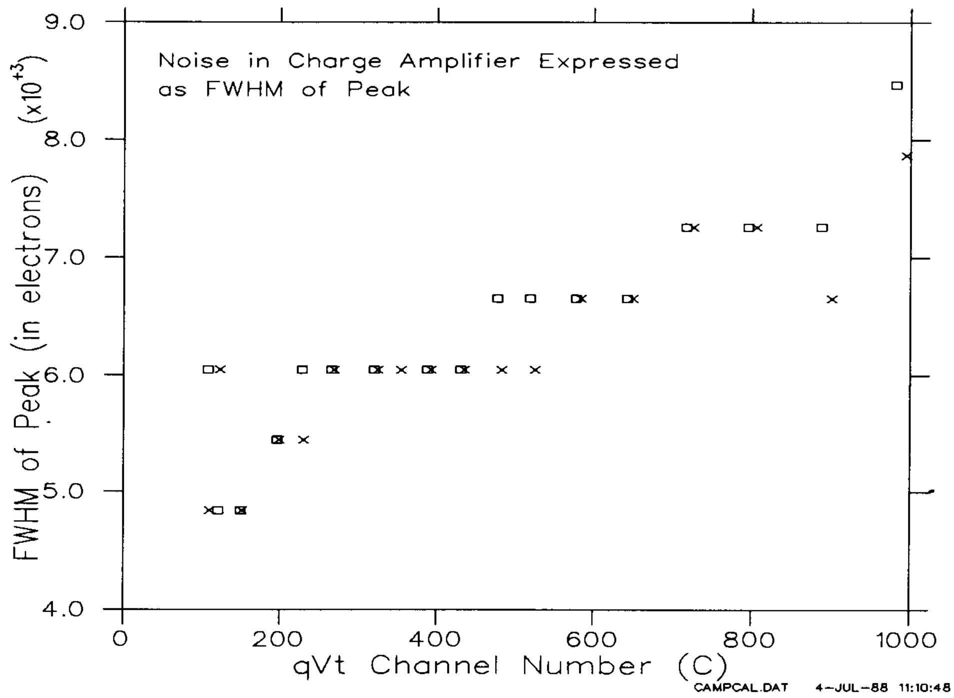

Figure 6.29: Noise in charge measuring system as a function of peak position.

6.2 Voltage Preamplifier Circuit

The charge sensitive amplifier system was used to collect spectra for heavily ionizing alpha particles, but was not sensitive enough to be used for detecting lighter ionizing ^{106}Ru electrons and minimum ionizing radiation. The primary reason for this was that the dual-in-line package (DIP) that the TPGD was mounted in, along with the DIP socket, added a capacitance of 3 pF to the output of the TPGD. This resulted in the signal being well immersed in noise. To overcome this problem an FET was wire bonded to the output of the TPGD inside the package, and operated as a source follower. Figure 6.30 is a schematic of the amplifying circuit used to detect minimum ionizing radiation. The second FET inside the package (Q2) was used to reset the TPGD output and has been replaced by a 150 kΩ resistor. Outside the package another source follower (Q3) drives the input of a modified wire chamber amplifier[2], which feeds into a NE5539 op-amp. The output of this circuit to a test pulse input is shown in Figure 6.31, and a calibration graph is given in Figure 6.32. The best resolution obtained with this amplifier was 0.1 mV at the input, or approximately 800 electrons, when using the pulse generator.

6.3 Data Acquisition Systems

Two different Data Acquisition Systems were used to compile histograms of pulse heights. On the test bench where ^{241}Am and ^{106}Ru sources were used, a LeCroy 3001 qVt was used, whereas for in-beam tests, a LeCroy 2249A ADC was used in conjunction with the STAR acquisition system [32] resident in the M11 counting room (see Section 7.3).

The Lecroy 3001 qVt is a multichannel analyser capable of functioning in charge,

[2] TRIUMF DRW #P1635

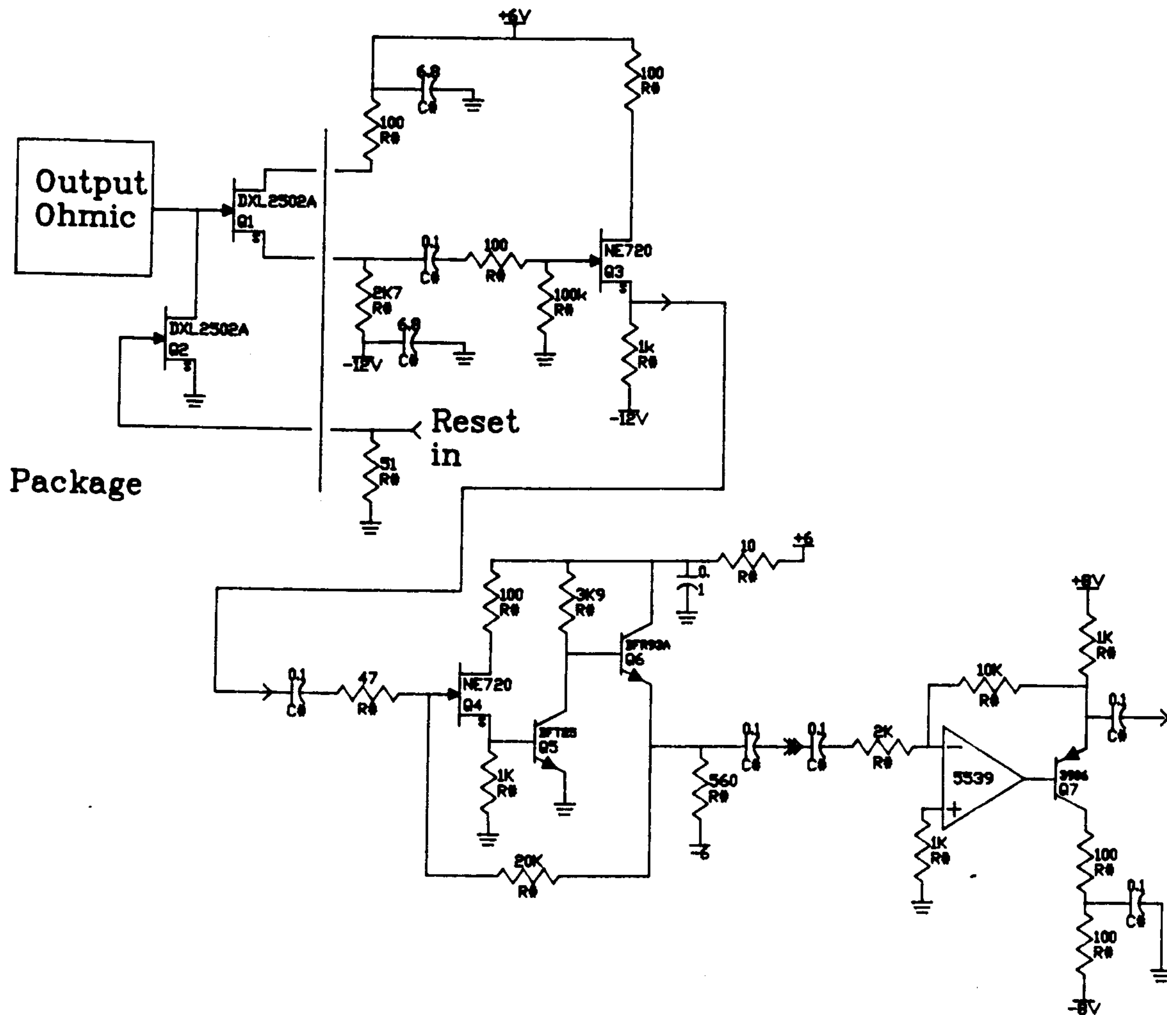

Figure 6.30: Schematic of voltage sensitive amplifier system.

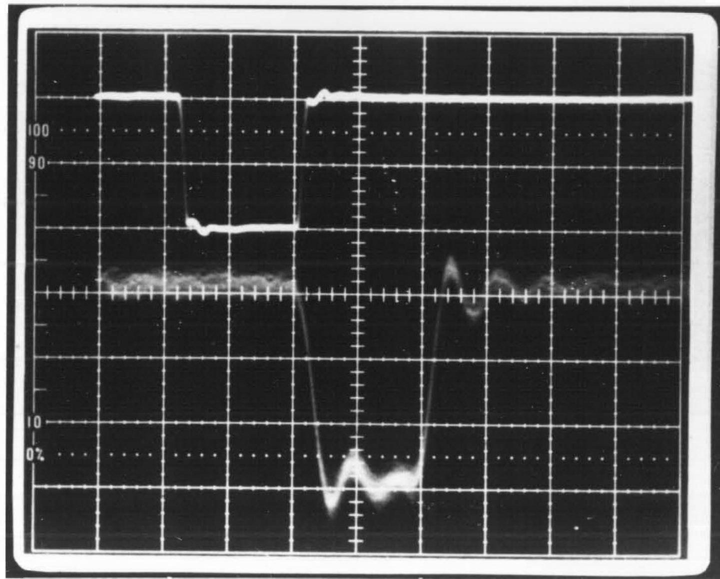

Figure 6.31: Response of voltage amplifier to test pulse. Scale is (upper trace) 500 mV/div, 20 ns/div; (lower trace) 50 mV/div, 20 ns/div. The input (upper trace) is attenuated by -60 db before being amplified.

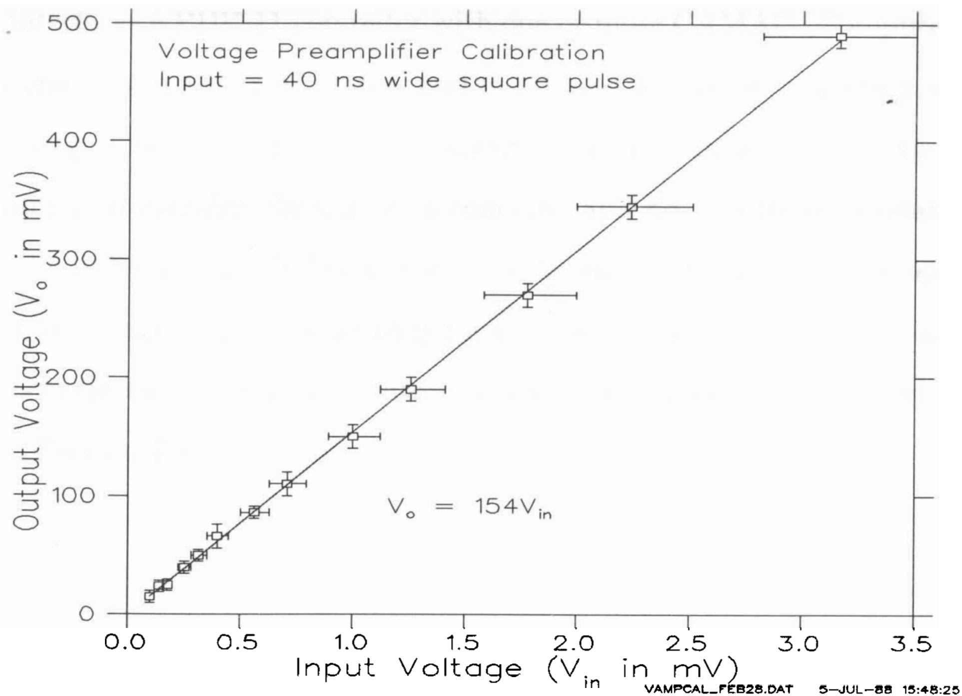

Figure 6.32: Calibration of voltage sensitive amplifier.

voltage, or time (start to stop) modes. When used with the Ortec 109A preamplifier (and a Tennelec TC205A shaping amplifier), the qVt was operated in V mode, which senses positive peaks in voltage. The V input of the qVt is designed for relatively slow pulses (rise times greater than 50 ns), and is not suitable for use with the other two amplifiers built at TRIUMF. An internal trigger with adjustable discriminator level is used to start a gating pulse of variable width, within which a peak voltage value is detected. When used with the TRIUMF amplifiers, the qVt was operated in q-mode to take advantage of the fast rise times of the pulses, and the 50 Ω impedance of the q-input. Again an internal discriminator was used to trigger a gate, during which the current into the q-input is integrated. By keeping this gate short ($<$ 100 ns) and varying the gain of the amplifiers, it is possible to get an accurate measure of the peak amplitude of the signal pulse.

The STAR Data Acquisition System is a program developed by Greg Smith [32] which interfaces a PDP-11 computer with one or more CAMAC (Computer Automated Measurement and Control) crates, and is tailored for use in collecting and analysing data during a particle physics experiment. The system gives the experimenter the opportunity to examine data as it is collected and do real time correlations between any of the different signals being examined by the system. When testing the TPGD, it was particularly useful for identifying the various particles incident on the TPGD, independently from the TPGD output signals. A discussion of how this was done in given in Section 7.3.

Chapter 7

Radiation Detection

The TPGD was tested with ^{241}Am α-particles, ^{241}Am γ-rays, ^{55}Fe X-rays, ^{106}Ru β-particles, and 292 MeV/c protons and pions. All except the ^{55}Fe X-rays were detected with varying degrees of efficiency. The ^{55}Fe X-rays have an energy of 5.9 keV and should produce up to 1400 electrons in the detector. This is below the noise threshold of the charge preamplifiers, and close to that of the voltage preamplifier. It is also half the charge expected from minimum ionizing radiation. The 60 keV ^{241}Am γ-rays were the first particles detected with the TPGD, but were not investigated in detail. The response of the detector to the other sources is discussed below.

7.1 Alpha Particles

Both charge preamplifier configurations (Section 6.1) were used to collect data for the ^{241}Am source[1]. The charging problems associated with the Ortec ac-coupled amplifier make that data unreliable and only the data from the TRIUMF amplifier is discussed. The FET input voltage sensitive preamplifier could not be used with the large alpha signals. Analog signals for all sources were viewed with either a Tektronics 7104 (1 GHz bandwidth) or 7904 (500 MHz bandwidth) oscilloscope frame, a high speed amplifier (Tek 7A29), and a Tektronics 7B92A time base. Data was collected with the TPGD, preamplifier and source inside a dark box. The geometry is shown in Figure 7.33. Alpha particle energy depends on the air thickness and the metallization on the TPGD. For

[1] 1 μC, uncollimated. All results were collected at room temperature

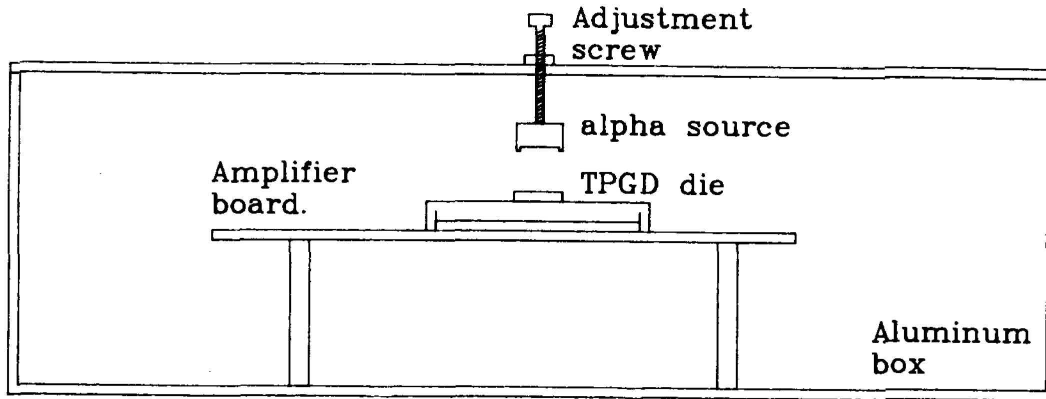

Figure 7.33: Geometry for collection of ^{241}Am data.

all energies considered, the energy loss in metallization is 0.2 ± 0.1 MeV, which along with the energy loss in air is calculated using the program XELOSS [33]. Incident alpha energy was varied by varying the air gap. This air gap will significantly reduce energy resolution (Section B.6). Table 7.4 gives the calculated incident alpha energy as a function of the air gap thicknesses for which spectra were obtained. Also included is the peak broadening expected as a result of the α-particle's passage through air.

Figure 7.34 is the response of the detector/amplifier to a 3.2 MeV alpha particle. The rise time is 6-7 ns and the RC of the tail is 1.3 μs. The pulse is sampled by the q-input of the qVt over the first 40 ns during which time the pulse approximates a DC step. Figure 7.35 is a typical spectrum for a large air gap and Figure 7.36 is a spectrum for a small air gap. For reference, Figure 7.37 [35] is the response of a commercial silicon detector to ^{241}Am (in vacuum). All alpha spectra for the TPGD exhibit poor energy resolution and extraneous peaks, indicative of incomplete charge collection over the designed radiation sensitive region [36,37,38]. This problem is independent of count rate (over the range of 120 to 14000 cpm), and appears to depend on alpha energy.

For the larger separations, the upper peak is quite well defined, and the number

Relative Source Position (turns)	Source to TPGD, separation (mm ±0.1 mm)	Calculated Alpha Energy (MeV)	Mean Alpha Range [34] (μm) (GaAs)	Calculated Peak Broadening (FWHM in MeV)
28	27	2.22	6.6	1.8
24	23.8	2.72	8.3	1.7
20	20.7	3.16	10	1.5
16	17.5	3.57	11	1.4
12	14.3	3.96	13	1.2
8	11.1	4.33	14	1.1
4	8.0	4.7	16	0.9
0	4.8	5.0	18	0.7

Table 7.4: Alpha energy as a function of air spacing.

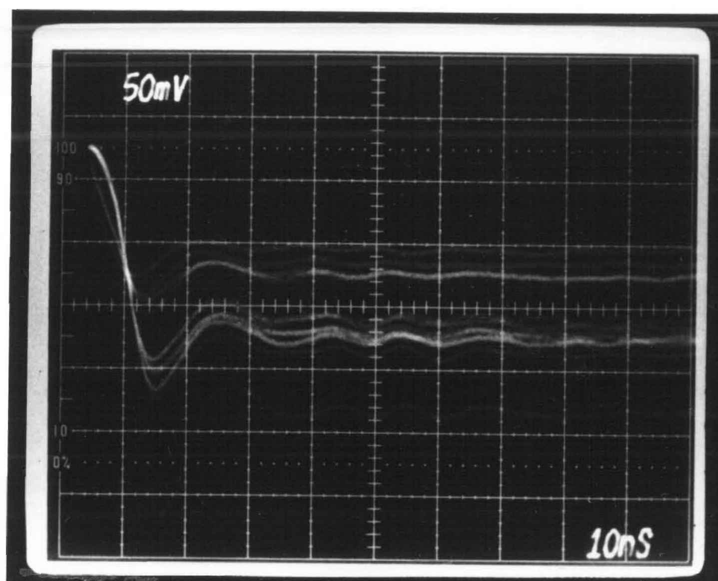

Figure 7.34: Response of TPGD/amplifier to α-particle. Scale is 50 mV/div, 10 ns/div.

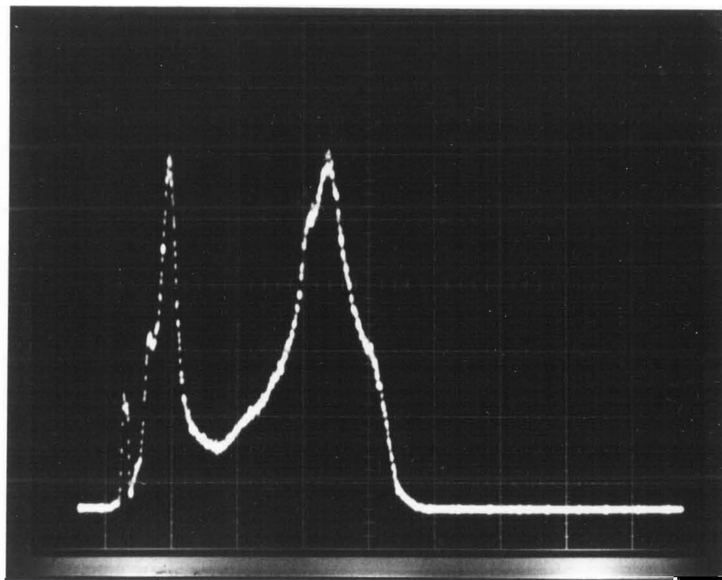

Figure 7.35: ^{241}Am α-particle spectra for an air separation of 27 mm.

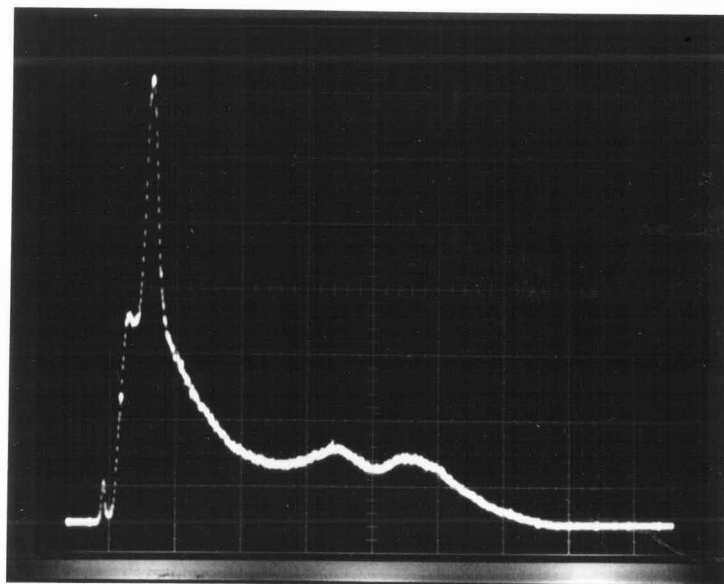

Figure 7.36: ^{241}Am α-particle spectra for an air separation of 8.0 mm.

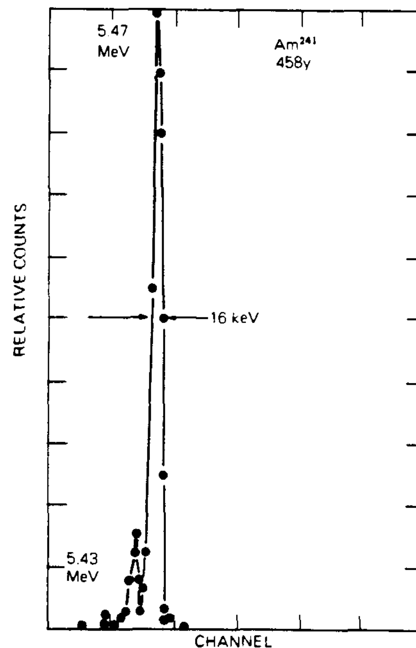

Figure 7.37: ^{241}Am α-particle spectra for a Si detector (in vacuum) [35].

of electrons collected that it represents was calculated. The channel position and the equivalent number of electrons collected for the upper peak for various source/TPGD separations is given in Table 7.5. The ehp creation energy $w_{\alpha,lab}$, as calculated for each separation is also given in the table. The number of electrons collected is plotted in Figure 7.38 as a function of calculated incident alpha energy. The inverse slope of this graph is another measure of the ehp creation energy, $w_{\alpha,graph}$. The variation in $w_{\alpha,lab}$ can be explained in terms of prompt recombination along the α-particle track in the GaAs [16,15]. As the α-particle passes through the GaAs it leaves a column of charge with an initial diameter of $\sim$ 300 Å [39]. Approximately 50% of this charge resides in a central column of 40 Å in diameter. Because the alpha particle is heavily ionizing, the charge density along this column is very high, typically 50000 ehp/μm. This linear density is equivalent to a volume density in the centre of the track of $\sim 1.6 \times 10^{21}$ cm^{-3}.

At this charge density, Auger recombination is the dominant recombination mechanism (see Figure 1.1) and hence means of loss of signal charge. The Auger recombination lifetime of an electron is given by

$$\tau_{Auger} = \frac{1}{Cn^2} \qquad [15] \qquad (7.21)$$

where

n is the electron and hole density (ehp density), and

C is a constant ranging from $\sim 10^{-29}$ to 10^{-38} cm^{6}s^{-1}.

Hopkins and Srour [16] use a value of $C = 10^{-33}$ cm^6 s^{-1} to demonstrate the effect on carrier lifetime of Auger recombination. Using this value, $\tau_{Auger} = 400$ ps for the ehp densities in the central core of the column. This is an order of magnitude less than the calculated collection time in the TPGD, and it is expected that a significant percentage of the signal charge will recombine through Auger recombination along the α-particle track. Together with later recombination by band to band radiative processes, Hopkins and Srour estimate that 15% of the signal charge is lost to prompt recombination after the passage of a 5.0 MeV α-particle. They use this value to explain a collection efficiency of 85% of the expected signal. As the recombination rates depend on the ehp density along the track, the collection efficiency will vary with the incident particle's stopping power. For the α-particle energies considered, the stopping power decreases with increasing energy and recombination would be expected to be more important for the lower energies. This is contradictory to the experimental data which indicates $w_{\alpha,lab}$ increases with increasing energy. This lab value of $w_{\alpha,lab}$ will differ from the value w discussed in Section 1.2 in that $w_{\alpha,lab}$ is calculated from the collected charge, not the charge produced by the radiation, and is not corrected for recombination processes.

The increase in $w_{\alpha,lab}$ might be explained by considering the total charge produced in the TPGD, the range of the α-particles and the observed incomplete collection for

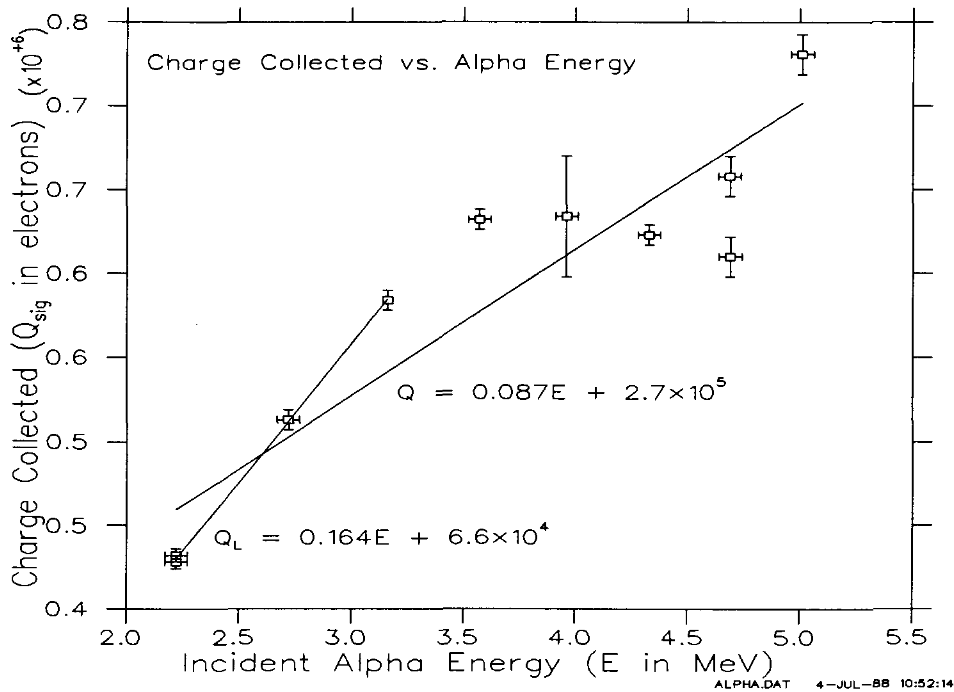

Figure 7.38: Signal charge collected as a function of α-particle energy.

Relative Source Position (turns)	Calculated Alpha Energy (MeV)	Upper Peak Channel Number and (FWHM)	Charge Collected (millions of e's)	EHP Creation Energy $w_{\alpha,lab}$ (eV)	Adjusted ehp Creation Energy $w_{adjusted}$ (eV)
28	2.22	420±3 (120)	0.428±0.004	5.2	4.4
28	2.22	423±3 (?)	0.432±0.004	5.1	4.4
24	2.72	490±5 (140)	0.513±0.006	5.3	4.5
20	3.16	549±5 (140)	0.584±0.006	5.4	4.6
16	3.57	588±5 (150)	0.632±0.006	5.6	4.8
12	3.96	590±30 (?)	0.630±0.04	6.2	5.3
8	4.33	581±5 (?)	0.623±0.006	7.0	5.9
4	4.69	570±10 (?)	0.610±0.01	7.7	6.5
4	4.69	610±10 (?)	0.660±0.01	7.1	6.1
0	5.01	670±10 (?)	0.730±0.01	6.9	5.8

Table 7.5: Charge collected in the TPGD for incident alpha particles.

some α-particles. As explained earlier, the column of ehp's produced will destroy any drift field in the region of the device. While this field is reforming, charge could be lost by diffusion, particularly for the more penetrating radiation, to regions from where it can not later be collected. This is particularly true if the sensitive depth of the TPGD is less than the range of the more penetrating α-particles, rather than the designed 20μm. It should be noted at this point that the TPGD was not designed with alpha particle detection in mind, which would indicate the use of a higher doping density in the sensitive region. With a higher doping density, the effect of radiative and Auger recombination would be reduced [15,16]. When used for detecting minimum ionizing radiation the excess carrier densities are considerably less and recombination by radiation and Auger processes are insignificant.

To compare the data collected with the TPGD with that of Hopkins and Srour [16,37], a prompt recombination of 15 % was assumed in calculating the adjusted values of $w_{adjusted}$ given in Table 7.5. Only for low energy alphas is this value of $w_{adjusted}$ comparable with published values (Section B.2). The value of $w_{\alpha,graph}$ calculated from the slope of the graph is not dependent on the amount of recombination that occurs, as long as it is a constant percentage. The graph gives a value of $w_{\alpha,graph} = 6.1$ eV for low energy α-particles and 11 eV averaged over all points.

7.2 Ruthenium Electrons

A ^{106}Ru source was used to test the TPGD's ability to detect electrons. This source produces β-particles in an energy continuum extending up to 3.5 MeV (minimum ionizing). Testing was done in a similar rig to that used for alpha sources. The lid of the DIP was left on for these tests, and in some cases the scintillating fibre shown in Figure 7.39 was used. This fibre extends through a hole in the DIP and contacts the

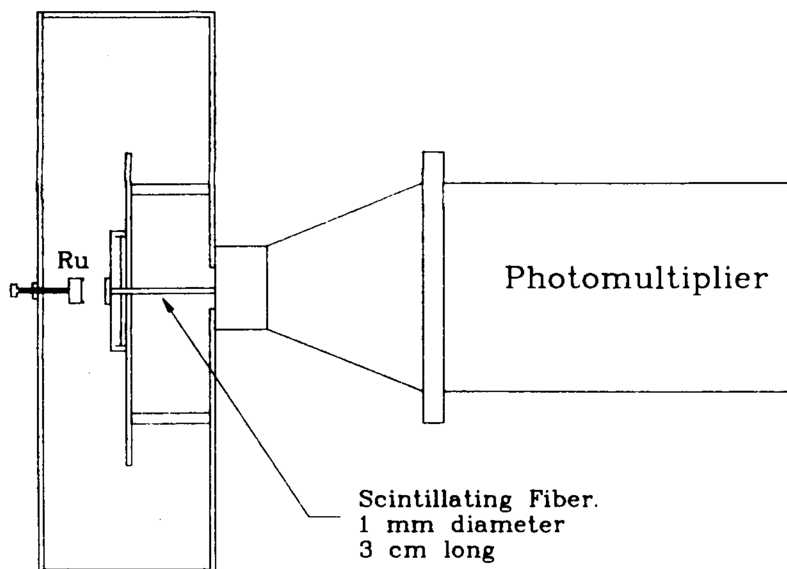

Figure 7.39: Geometry for measuring Ruthenium electrons.

backside of the die in line with the pixel being amplified by the voltage preamplifier. Other pixels were grounded. The output of the voltage preamplifier/TPGD for a ^{106}Ru electron is shown in Figure 7.40, and a pulse height spectrum obtained with a qVt triggered off the TPGD output is shown in Figure 7.41. The pulse from the TPGD shows a decay time constant of (80 ± 10) ns, giving a capacitance at the TPGD output/FET input of (530 ± 70) fF; slightly more than the capacitance of the TPGD die itself. The spectrum shows the expected tail for an energy continuum; however this is probably due in part to incomplete charge collection. It was not possible to establish a coincidence between the TPGD and the scintillating fibre, indicating that the pulses observed were due to non-minimum ionizing particles. A slight misalignment between the pixel of interest and the scintillating fibre may have aggravated this problem, as minimum ionizing particles were observed with the TPGD in a pion beam.

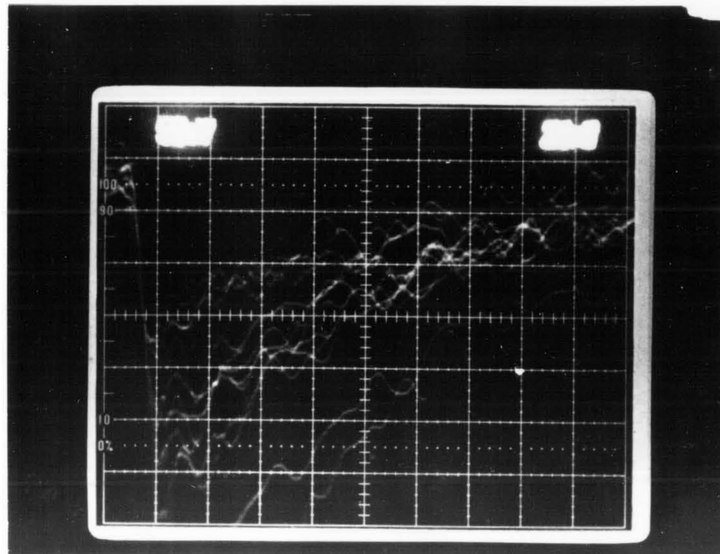

Figure 7.40: Response of voltage preamplifier to ^{106}Ru electrons. Scale is 50 mV/div, 20 ns/div. RC of tail is 80 ± 10 ns.

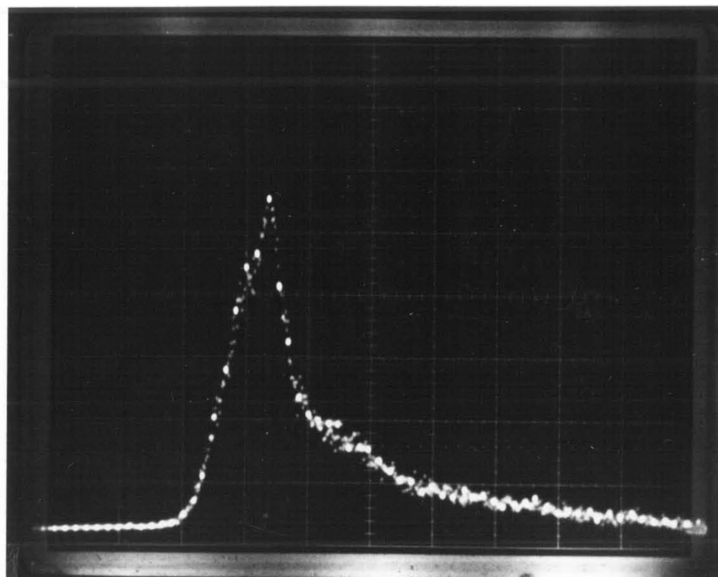

Figure 7.41: ^{106}Ru spectra from the TPGD. Lower edge is discriminator cutoff. Tail is typical of energy continuum.

7.3 Protons and Pions

Testing of the TPGD with 292 MeV/c protons and pions took place in the M11 experimental area off of beam line 1A on the cyclotron at TRIUMF. The M11 channel, together with target T1 is designed for production of 50 to 300 MeV pions, and when run with positive polarity, contains approximately 10 protons for every pion. Particle energy is selected by adjusting the momentum acceptance of the channel's dipole magnets and horizontal slit opening. A more detailed description of M11 is given in the TRIUMF Users Handbook [40].

The TPGD was initially placed in the beam as a parasitic experiment, but like all good parasites quickly took over the experimental area. The data presented below was collected with the STAR acquisition system over a run time of 20 hours. Figure 7.42 shows the experimental set-up. The first scintillator is a piece of scintillating fibre with a cross section perpendicular to the beam of 1 mm × 1mm, and a thickness of 2 mm. The backside scintillator has a cross section of 1" × 1" and a thickness of 1/8". The energy resolution of the fibre was extremely poor, while that of the larger scintillator was suitable for distinguishing protons from pions. The mean particle momentum was fixed at 292 MeV/c for the experiment, while the momentum acceptance was allowed to vary from 1 to 5 % by varying the slit widths. Protons were obtained by leaving out the absorber in the beam line. Data collected were grouped into 14 runs for histogramming purposes.

7.3.1 Data Collection

Signals from both scintillators and the TPGD were fed into the M11 counting room where they were split by a linear Fan-in-Fan-out (Lecroy 428F) and then taken to a LeCroy 2249A ADC, through appropriate delay lines and attenuators. A logic signal

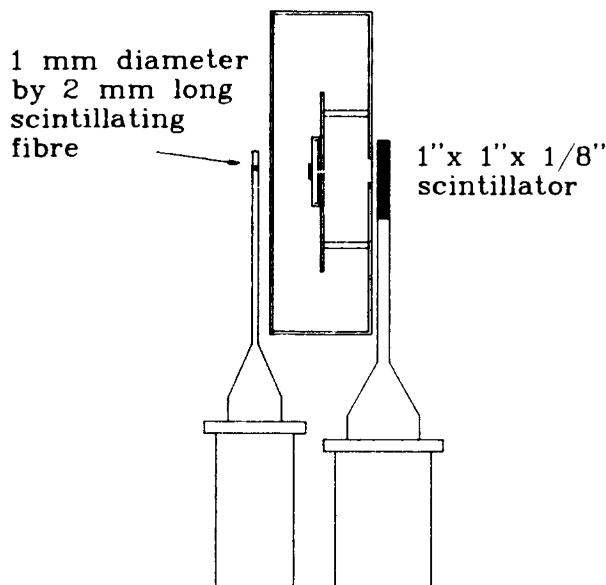

Figure 7.42: Geometry of M11 experiment.

obtained from each of the 3 sources was used together with a logic signal derived from the cyclotron RF to identify a valid event and do coincidence measurements for such an event. A valid event was defined as a particle detected passing through both scintillators and the TPGD. The STAR system gated (140 ns gate) the ADC on for a valid event and recorded the peak amplitude of the pulses from the three detectors. The acquisition system also counted the total number of counts over a run for each detector, as well as the number of specified coincidences. Using the subprogram CUTS of the STAR system, protons were discriminated from pions by either time-of-flight or signal amplitude in the large scintillator.

7.3.2 Results

Two types of data were collected for analysis:

1. Total counts and selected coincidences for determining efficiencies.

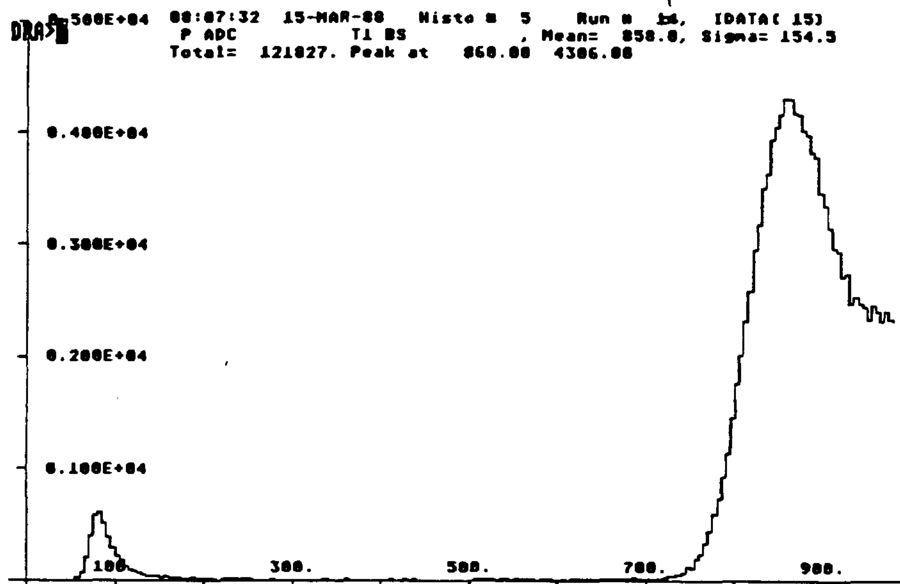

Figure 7.43: Spectra of large scintillator (without proton absorber).

2. Peak amplitudes of pulses from each of the three detectors for a valid event, for determining energy spectra.

The pions in the beam are minimum ionizing and deposit 14 keV of energy in 20 μm of GaAs, while the protons deposit 100 keV in the same thickness (see Section B.7).

The histogram in Figure 7.43 shows the pulse heights observed in the large scintillator when both protons and pions are present in the beam. Those events occurring below channel # 250 were labelled as pions for the purpose of examining the TPGD spectrum, while those above # 300 were labelled as protons. The TPGD spectra for the same run is shown in Figure 7.44 before applying the proton/pion cut, and in Figure 7.45 after application of the CUTS program. Similar histograms for a run where the proton absorber was inserted in the beam are shown in Figures 7.46, 7.47, 7.48. Together these histograms show the TPGD's ability to detect minimum ionizing radiation, although with obvious low efficiencies.

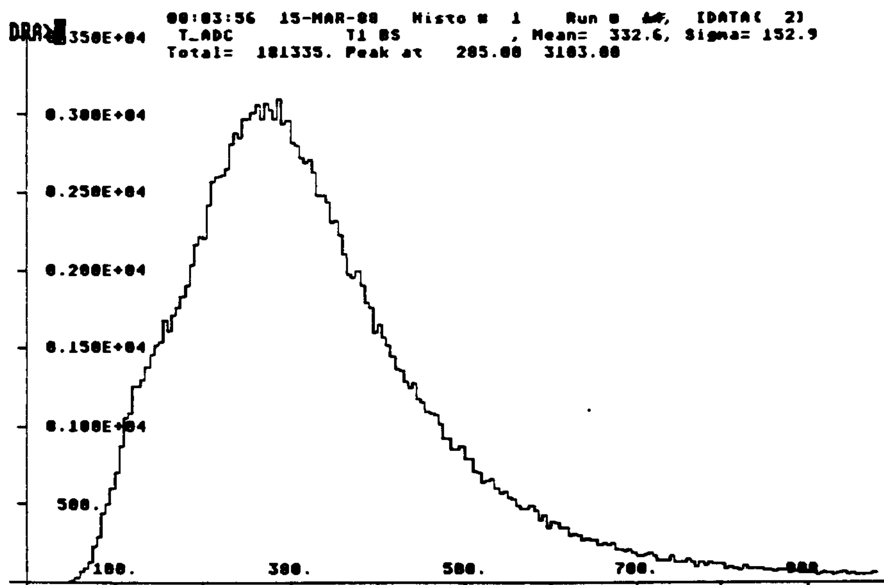

Figure 7.44: Histogram of TPGD for 292 MeV/c protons and pions.

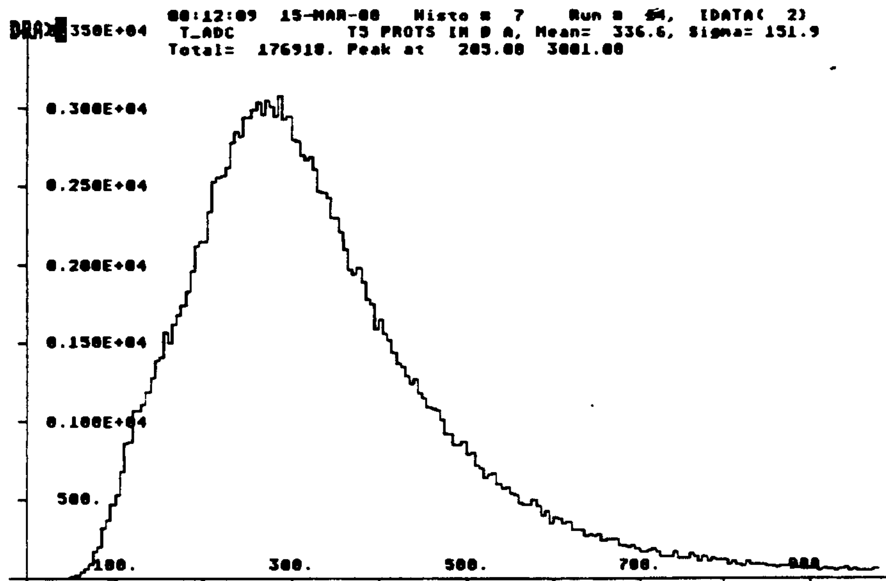

Figure 7.45: Proton spectra of TPGD after STAR CUTs.

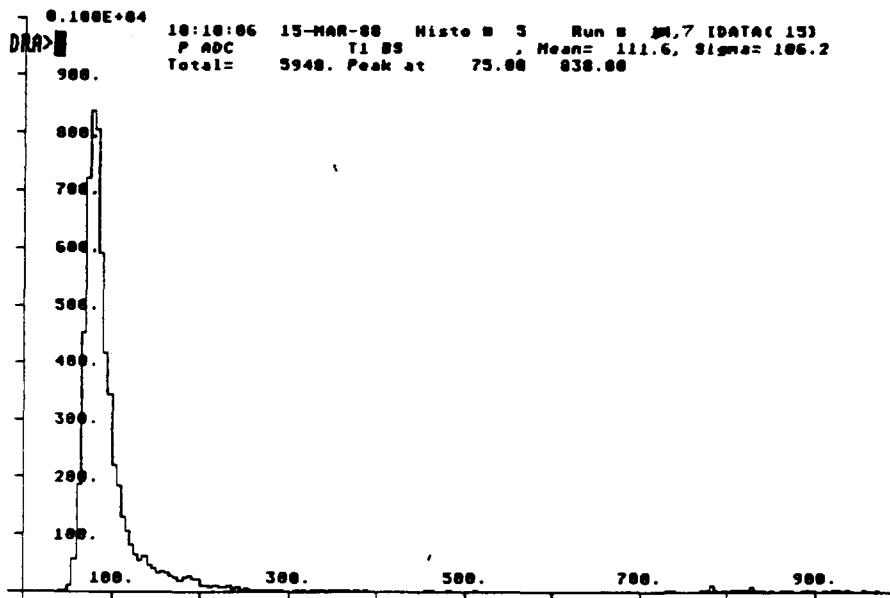

Figure 7.46: Spectra of large scintillator (with proton absorber).

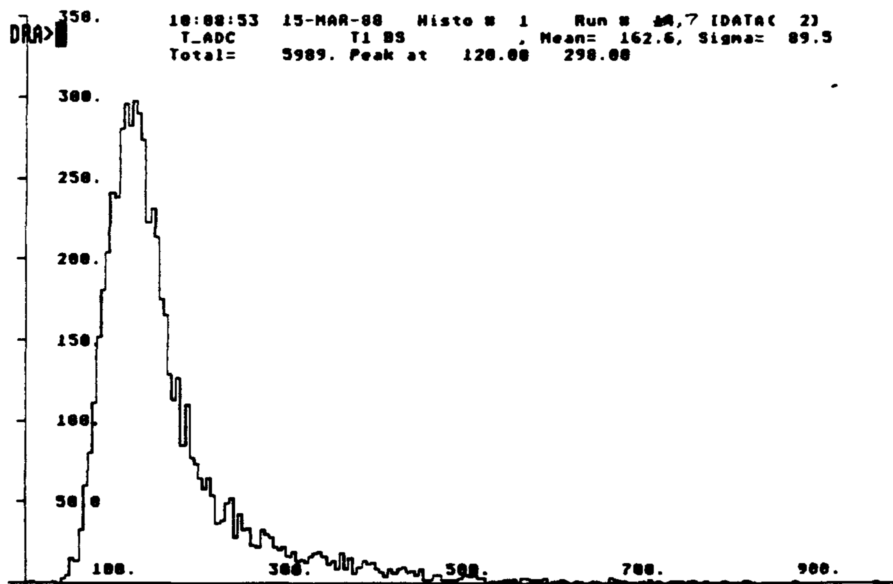

Figure 7.47: Histogram of TPGD for 292 MeV/c pions.

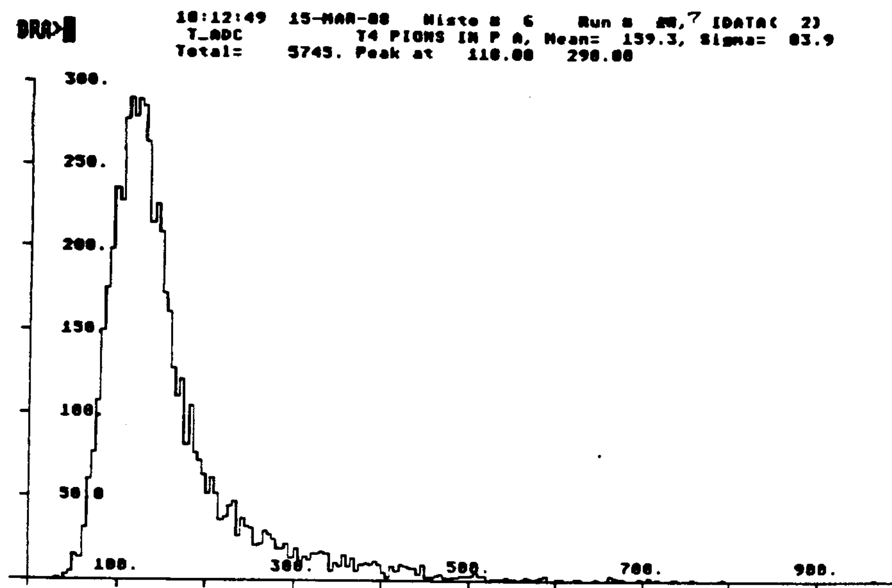

Figure 7.48: Pion spectra of TPGD after STAR CUTs.

The efficiency of the TPGD was calculated relative to that of the scintillating fibre for all 14 runs. No discrimination between the efficiency of proton and pion detection within a given run was attempted. Both the fibre and the single pixel of the TPGD from which data were collected are approximately the same size and were aligned to within 0.5 mm of each other on the beam axis. The TPGD efficiency is given by:

$$\frac{T \cdot P}{S \cdot P} \times \frac{A_S}{A_T} \times 100\% \tag{7.22}$$

where

$T \cdot P$ is the coincidence between the TPGD and the large scintillator (P),

$S \cdot P$ is the coincidence between the fibre (S) and the large scintillator, and

A_T, A_S are the cross sectional areas of the TPGD and fibre respectively.

This efficiency is plotted in Figure 7.49. For beams high in protons the efficiency is $9 \pm 1\%$, while for pion beams the efficiency is $0.8 \pm 0.2\%$.

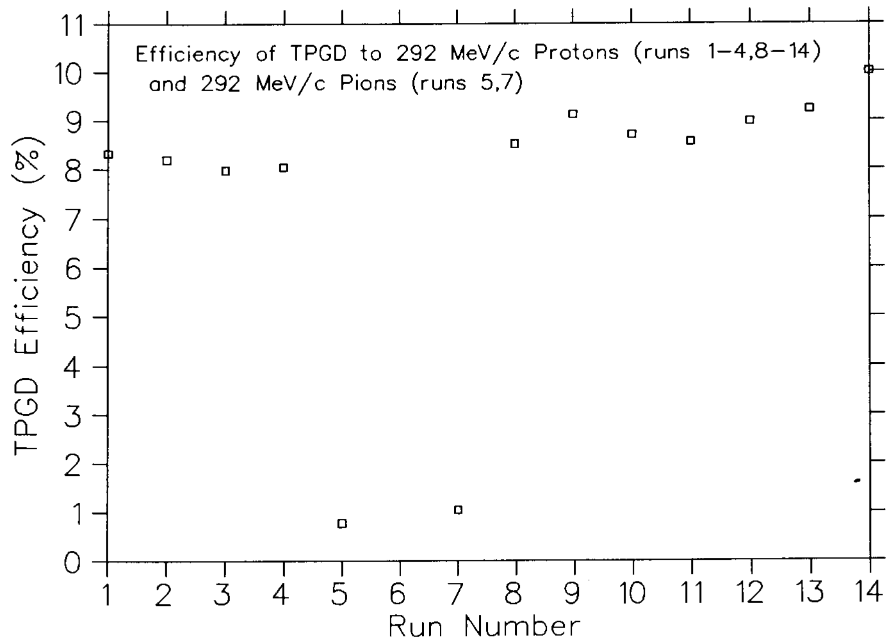

Figure 7.49: Calculated efficiency of TPGD to 292 MeV/c protons and pions. Runs 5 through 7 were done with the proton absorber in place.

An absolute energy calibration of the acquisition system for this experiment was not attempted at the time, as energy resolution was not then of interest. However, neglecting losses in the cabling between the experimental area and the counting room, an approximate energy calculation can be performed. Pulse amplitudes from the discrimination threshold to over 800 mV were observed (Figure 7.50). The measured RC of the decay of these pulse was 106 ns; equivalent to a detector plus FET capacitance of 710 fF. For this capacitance at the input of the amplifier, the signal charge is approximately:

$$Q_{sig} = \frac{0.71 \times 10^{-12} \times V_o}{A} \tag{7.23}$$

where

V_o is the output voltage of the amplifier and,

A is the gain of the amplifier = 154.

For a 1 V pulse, the signal charge is 29000 electrons equivalent to 120 keV deposited in the GaAs. This is in agreement with the calculated 100 keV expected from the protons. The histograms can be (energy) calibrated using data obtained by placing a variable DC voltage source on the input of the acquisition system (in the counting room) and approximating the signal pulse by an exponential decay:

$$V(t) = V_{peak} \exp^{\frac{t}{106}}$$

Integrating the DC voltage and the modeled voltage over the gate length of the ADC (140 ns), and equating the two values:

$$\int_0^{140} V_{peak} \exp^{\frac{t}{106}} dt = \int_0^{140} V_{DC} dt \tag{7.24}$$

gives

$$V_{peak} \simeq 5 V_{DC}$$

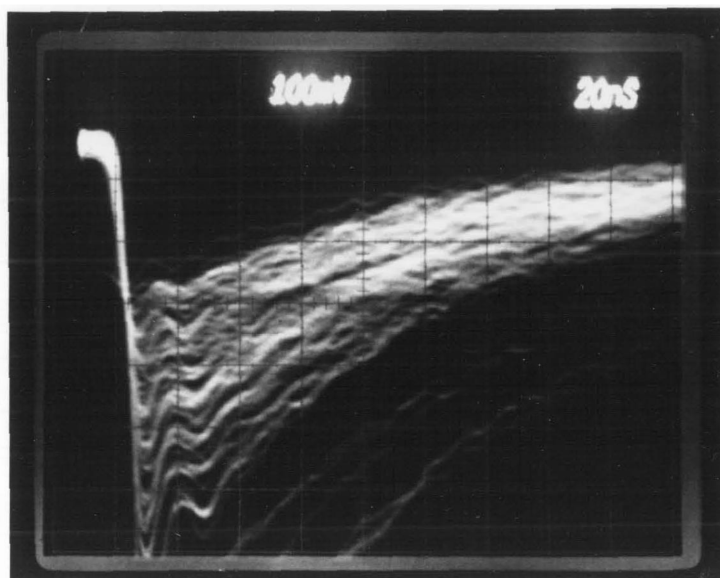

Figure 7.50: Response of TPGD/amplifier to protons and pions. Scale is 100 mV/div, 20 ns/div. RC of tail is 105 ± 5 ns.

The energy calibration of the acquisition system is then shown in Figure 7.51. For a peak at channel number 285 (average for protons) the peak voltage amplitude from the amplifier is approximately 350 mV; equivalent to a collected charge of 10000 electrons (42 keV). For pions, the average peak position was 105 ± 15; equivalent to 3000 electrons (13 keV). It is apparent that for the pions detected, almost all of the charge was collected, while on average for the protons, approximately half the expected charge was collected.

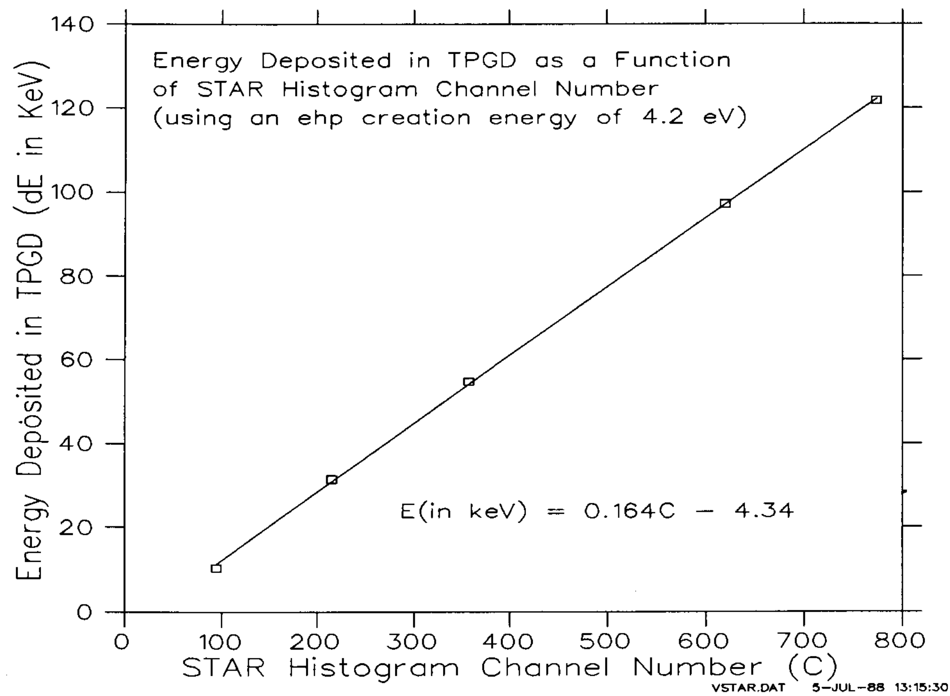

Figure 7.51: Calibration of STAR histograms in terms of energy.

Chapter 8

Conclusion

8.1 Alpha Particles

An ehp production energy ranging from w = 4.4 eV to 6.5 eV for incident alpha particle energies ranging from 2.22 MeV to 5.0 MeV was calculated assuming a prompt recombination of 15 % of the charge produced in the TPGD. These values neglect any loss of signal charge to later recombination or trapping processes, or to non-sensitive regions of the TPGD.

Incomplete charge collection was observed for some particles at all energies investigated, although it is most prevalent for high energies. This indicates that the TPGD is not uniformly sensitive over its designed area, and in particular that it's sensitivity varies with depth. Whether this is due to regions of high trapping centre densities, or non-depletion, or other reasons, is not known. To further investigate the spatial sensitivity of the TPGD, a means to precisely position a signal charge must be used. This might be done with a high energy electron beam, or a highly collimated, variable energy alpha source. Furthermore, if the TPGD structure is to be used for detecting alpha radiation, it should be fabricated on a more highly doped epitaxial layer to alleviate problems with Auger and radiative recombination. This would entail modifying the design of the TPGD in light of the high fields that would be present. As the TPGD was not designed for alpha spectroscopy it is not recommended that this be pursued with the present design.

8.2 Protons and Pions

The ability to detect minimum ionizing radiation with the TPGD was demonstrated with 292 MeV/c pions obtained from the M11 experimental area of the cyclotron at TRIUMF. The efficiency of detection was very low (0.8%) compared with a similarly sized scintillating fibre. Protons of the same momentum were detected with a 9% efficiency during the same experiment. For the pions detected, the charge collected was (on average) that expected from design calculations. For the protons, the average charge collected was approximately half that expected. Together, the low efficiencies and the complete charge collection for pions indicate that TPGD is sensitive over only a very small portion of its designed radiation detection region.

8.3 Summary

The work presented indicates that it is possible to detect minimum ionizing radiation in a 20 μm GaAs epitaxial layer on a semi-insulating substrate. The efficiency of detection was disappointingly low, and appears to be due to incomplete charge collection from almost all of the designed sensitive region of the device. This needs to be investigated with a precisely positionable source such as high energy electron microscopy.

Problems with the mask design should be corrected for future devices, and tighter control over the quality of the epitaxial layer should also be exercised.

Appendix A

Fabrication Routine

Processing routine for the TPGD

1. Start with one quarter of the Raytheon 15T690 GaAs wafer. This wafer has a nominally undoped epitaxial layer 20 μm thick. Polaron measurements by Raytheon indicate a doping density less than 1×10^{14} cm^{-3}. A highly doped $N^+ = 1.1 \times 10^{18}$ cm^{-3} layer, 0.22 μm thick, was grown on the surface to improve ohmic contacts.
2. Clean and degrease wafer in trichloroethylene, acetone and 2-propanol.
3. Light clean-up etch on surface with a NH_4OH:H_2O_2:H_2O solution.
4. Dry with 2-propanol and N_2.
5. Spin on photoresist and softbake.
6. Align and expose layer L01 (N^+ etch) to $< 100 >$. Develop photoresist.
7. Etch N^+ layer in NH_4OH:H_2O_2:H_2O.
8. Reclean wafer in acetone and 2-propanol.
9. Spin on photoresist and softbake.
10. Align and expose layer L03 (ohmic metallization) to N^+ etch. Develop photoresist.
11. Light clean-up etch on surface with a NH_4OH:H_2O solution.

12. Vacuum deposit 1100 Å of AuGe (12% Ge), 100 Å of Ni and 1400 Å of Au.
13. Liftoff ohmic metal and photoresist in acetone and/or pyrrolidone.
14. Reclean wafer in acetone and 2-propanol.
15. Alloy in tube furnace at 450 °C.
16. Reclean wafer in acetone and 2-propanol.
17. Spin on photoresist and softbake.
18. Align and expose layer L05 (Schottky metallization) to ohmic metal. Develop photoresist.
19. Light clean-up etch on surface with a NH_4OH:H_2O solution.
20. Vacuum deposit 500 Å of Ti, 100 Å of Pt, and 2100 Å of Au.
21. Liftoff Schottky metal and photoresist in acetone and/or pyrrolidone.
22. Reclean wafer in acetone and 2-propanol.
23. (Optional) Spin on polyimide and soft cure.
24. Spin on photoresist and softbake.
25. Align and expose layer L06 (vias) to ohmic metal. Develop photoresist and (optionally) polyimide.
26. Light clean-up etch on surface with a NH_4OH:H_2O solution.
27. Vacuum deposit 500 Å of Ti, and 2100 Å of Au.
28. Liftoff second level metal and photoresist in acetone.

29. Reclean wafer in acetone and 2-propanol.

30. (Optional) Fully cure polyimide.

Appendix B

Design Calculations

B.1 Epitaxial Layer Thickness

The thickness of the epitaxial layer will determine the amount of charge that will be produced by ionizing radiation, as well as the capacitance, leakage currents, and time response of the device. Depending on the doping of the layer, the voltage required to deplete the epitaxial layer from a reverse biassed Schottky diode, is found by solving Poisson's equation (in one dimension):

$$\nabla \cdot \vec{E} \equiv \frac{\partial E}{\partial x} = \frac{\rho(x)}{\epsilon_s} = \frac{q}{\epsilon_s}\left[p(x) - n(x) + N_D^+(x) - N_A^-(x)\right] \tag{B.25}$$

where ϵ_s is the permittivity of the semiconductor $= \epsilon_r \epsilon_0$ (ϵ_r(GaAs) $= 12.9$)
$n(x)$ is the electron concentration,
$p(x)$ is the hole concentration,
N_D^+ is the donor concentration,
N_A^- is the acceptor concentration, and
x is the depth into the epitaxial layer, with the surface being at $x = 0$.
If the epitaxial layer is to be depleted to a depth, w, then for $x < w$, N_D^+ is much greater than the other concentrations. For $x > w$, there is no field and $\rho_{net} = 0$. Then Equation B.25 reduces to:

$$\frac{\partial E}{\partial x} = \frac{q}{\epsilon_s} N_D \qquad \text{for } 0 < x \leq w \tag{B.26}$$

$$= 0 \qquad \text{for } x > w \tag{B.27}$$

Solving this while taking $E(x = w) = 0$ as a boundary condition, gives:

$$E(x) = \frac{qN_D}{\epsilon_s}(x - w) \qquad \text{for } 0 < x \leq w \tag{B.28}$$

The potential of the system, ψ, is found by integrating again to get (taking $\psi(x = w) = 0$ as a boundary condition):

$$\psi(x) = \frac{qN_D}{2\epsilon_s}(x^2 - 2wx + w^2) \qquad \text{for } 0 < x \leq w \tag{B.29}$$

Thus to deplete to a depth w, a voltage of $V = \frac{qN_D}{2\epsilon_s}w^2$ is required. The voltage, V, should include the built-in voltage, V_{bi}, resulting from the Schottky junction [19,26,27], as well as the applied voltage $V_{applied}$.

$$V = V_{bi} + V_{applied} = \frac{qN_D}{2\epsilon_s}w^2 \tag{B.30}$$

The built-in voltage of a Schottky barrier on GaAs varies in a not well understood manner, depending on the technique used to form the junction, as well as on the condition of the semiconductor surface and the type of metallization used. A good discussion on the nature of metal-semiconductor junctions can be found in a book by Sharma [27], or by Rhoderick [41], as well as in various papers (for example [26,42,43]). For modelling purposes, V_{bi} was taken as 0.8V. Table B.6 gives the depletion depth for various doping densities, N_D, and voltages, V. It also contains the maximum electric field in the depletion region. The breakdown field strength for 1×10^{14} cm^{-3} material is ≈ 300 kV/cm, and slightly higher for higher dopings [19].

To maximize the depletion depth, and hence signal, a minimum doping level is required. For commercially available epitaxial material, this is approximately equal to $N_D = 1 \times 10^{14}\text{cm}^{-3}$. Starting from this point, an expected signal charge can be calculated for various depths and traded off against the voltage required to obtain depletion.

Depletion Depth (μm)	Doping Density, N_D (cm^{-3})	Depletion Voltage, V_D (V)	Maximum Field, E_{max} (kV/cm)
3.4	1×10^{14}	0.8	4.6
10	1×10^{14}	7.0	14
20	1×10^{14}	28	28
50	1×10^{14}	175	70
20	1×10^{13}	2.8	2.8
20	5×10^{13}	14	14
20	5×10^{14}	140	140
20	1×10^{15}	280	280

Table B.6: Depletion depths for various doping densities and voltages

B.2 Signal Size

The expected signal for minimum ionizing radiation can be calculated as the charge deposited in the depletion region of the detector. This depends on the stopping power of the gallium arsenide, which because of the dependence on the atomic number of the material (see Equation 1.2), is very close to that of germanium. Minimum ionizing radiation in germanium has a stopping power of approximately,

$$\frac{dE}{d(\rho x)} = 1.2 \quad \text{MeV g}^{-1}\text{ cm}^2 \qquad [2,44] \qquad \text{(B.31)}$$

$$\text{or} \quad \frac{dE}{dx} = 6.4 \quad \text{MeV cm}^{-1} \qquad \text{(B.32)}$$

where $\rho = 5.32$ g cm^{-3} is the density of GaAs.
For the thickness of interest, this energy loss rate is constant.

Given the stopping power, the number of electron hole pairs (ehp's) produced is found by dividing by the energy required to produce an ehp in GaAs. For GaAs, experimental values range from 4.2 to 5.2 eV [6, 5.0 eV], [45, 4.68 ± 0.14 eV], [16, 4.8 eV], [10, 4.27 ± 0.05 eV], [5, 4.2 eV], [28, 4.2 eV], [46, 4.7 eV]. A value of 4.2 was used in calculations as it seems reasonable that the lower the value of w, the more efficient the conversion must have been (worst case is 24% higher). The expected ehp yield is

then approximately 150 per micron. For a 20 micron epitaxial layer this is 3000 ehp's or 0.48 fC of charge. Note that each ehp contributes only one elementary charge unit to the total signal, as the electron drifts to one electrode and the hole to the other resulting in a net *transfer* across the depletion region of one elementary charge.

B.3 Structure Capacitance

Considering the equivalent circuit of a diode semiconductor detector and the nature of the signal from such a device (see Chapter 6 and Figure 6.21), the capacitance of the output node should be calculated to determine the signal size expected. Fof an epitaxial GaAs layer in full depletion on an S.I. substrate this is equivalent to calculating the capacity of coplanar electrodes. If it were not for the semi-insulating substrate, or if the device is not operated in full depletion, the capacitance would be that of a parallel plate capacitor with a plate separation equal to the depletion depth. Such a device would have a capacitance so large that operation on a 20 micron epitaxial layer would not be possible.

The capacity of coplanar electrodes (see Figure B.52), is calculated by making a conformal mapping into a region where the electrodes form a parallel plate capacitor. This is done through two mappings. The first maps the z-plane into the z′ = z/a plane as shown in Figure B.52, and then uses a Schwarz-Christoffel to transform the right half of the z′ into the w-plane. This transformation takes the form:

$$\frac{dw}{dz'} = \frac{A}{(z'+b/a)^{1/2}(z'+1)^{1/2}(z'-1)^{1/2}(z'-b/a)^{1/2}} \tag{B.33}$$

Substituting $m = a/b$, and noting that $m < 1$ for all strip widths and separations,

$$\frac{dw}{dz'} = \frac{A}{(z'^2-1/m^2)^{1/2}(z'^2-1)^{1/2}} \tag{B.34}$$

$$= \frac{-mA}{(1-m^2z'^2)^{1/2}(1-z'^2)^{1/2}} \tag{B.35}$$

Noting that $z' = 1, 1/m$ are poles in this differential, integration is done separately over three regions:

1. $0 < z' < 1$
2. $1 < z' < 1/m (= b/a)$
3. $1/m < z'$

On region 1.

$$\int_0^1 dw_1 = \int_0^1 \frac{-mAdz'}{(1 - m^2 z'^2)^{1/2}(1 - z'^2)^{1/2}} \tag{B.36}$$

$$= -mAK(m) \tag{B.37}$$

where $K(m)$ is the elliptic integral of first order.

On region 2.

$$\int_1^{1/m} dw_2 = \imath \int_1^{1/m} \frac{mAdz'}{(1 - m^2 z'^2)^{1/2}(z'^2 - 1)^{1/2}} \tag{B.38}$$

$$= \imath mAK'(m) \tag{B.39}$$

where $K'(m)$ is the complementary elliptic integral of first order.

On region 3.

$$\lim_{R\to\infty} \int_{1/m}^{R} dw_3 = \lim_{R\to\infty} \int_{1/m}^{R} \frac{mAdz'}{(m^2 z'^2 - 1)^{1/2}(z'^2 - 1)^{1/2}} \tag{B.40}$$

take $mz' = 1/t$ to get

$$\lim_{R\to\infty} \int_{1/m}^{R} dw_3 = \lim_{R\to\infty} \int_{1}^{1/mR} \frac{-mAdz'}{(1/t^2 - 1)^{1/2}(1/(mt)^2 - 1)^{1/2}} \tag{B.41}$$

$$= \lim_{R\to\infty} \int_{1/mR}^{1} \frac{mAdt}{(1 - t^2)^{1/2}(1 - m^2 t^2)^{1/2}} \tag{B.42}$$

$$= mAK(m) \qquad \text{as } R \to \infty \tag{B.43}$$

This maps into the w-plane as shown in Figure B.53. From this an effective parallel plate configuration with plate width W' and separation S' can derived, where:

$$W' = mAK(m)$$
$$S' = mAK'(m)$$

The capacitance per unit length (neglecting fringing effects) of a parallel plate capacitor is

$$C = \epsilon \frac{W'}{S'} \quad \text{(B.44)}$$
$$= \epsilon \frac{K(m)}{K'(m)} \quad \text{(B.45)}$$

Considering that there is both air above the electrodes and semiconductor below, ϵ is given by:

$$\epsilon = (1 + \epsilon_s)\epsilon_o \quad \text{(B.46)}$$

The complementary elliptic integral $K'(m)$ can be written as

$$K'(m) = K(\sqrt{1 - m^2})$$

Then

$$C = (1 + \epsilon_s)\epsilon_o \frac{K(m)}{K(\sqrt{1 - m^2})} \quad \text{(B.47)}$$

The actual capacitance seen by the ohmic output is twice this (to account for the z< 0 plane). The elliptic integrals are implemented in a data manipulation program called OPDATA [47] which was used to produce Figure B.54 showing the ratio of

$$\frac{K(m)}{K(\sqrt{1 - m^2})}$$

for various ratios of W/S.

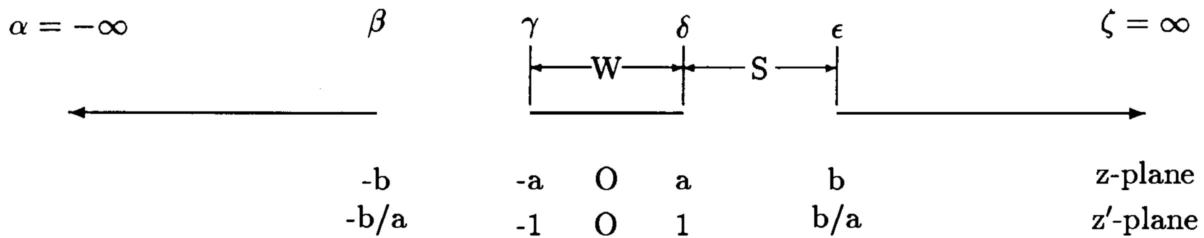

Figure B.52: Coplanar geometry of Schottky drift electrodes and ohmic output electrode. Drift electrode D6, on either side of the ohmic electrode, is the nearest electrode to the output electrode. It is taken together with the other drift electrodes as extending to ∞.

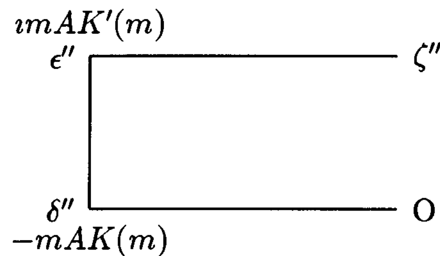

Figure B.53: Coplanar plates conformally mapped into parallel plates.

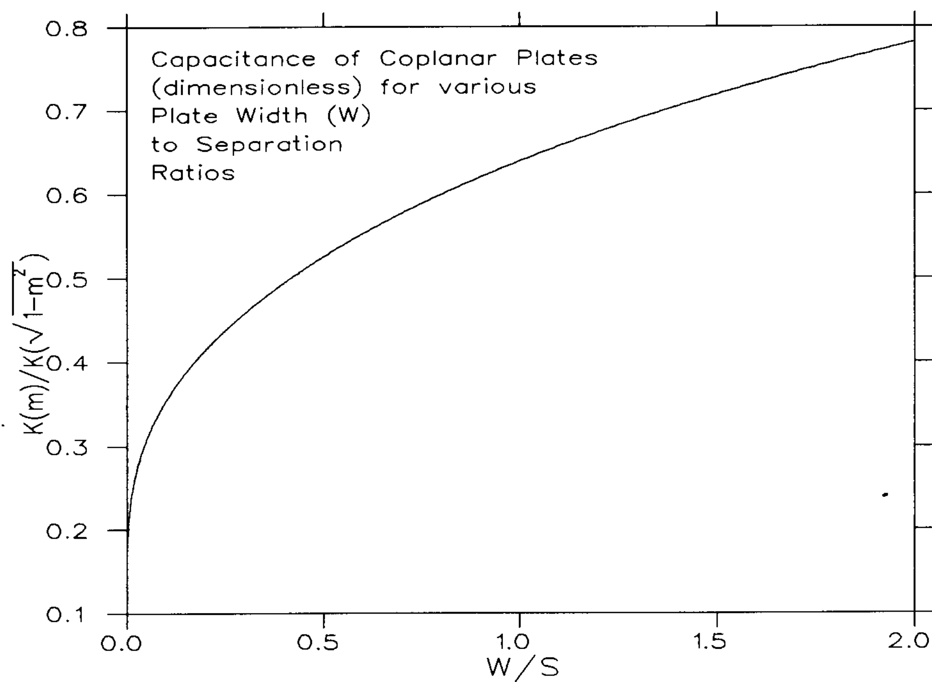

Figure B.54: Capacitance of coplanar plates.

W/S	K(m)/K'(m)	C_o (pF/cm)	C_f (fringing) (pF/cm)
0.1	0.355	.874	1.74
0.2	0.415	1.02	2.00
0.5	0.526	1.29	2.46
0.67	0.570	1.40	2.64
1	0.640	1.57	2.90
2	0.782	1.92	3.40
5	1.01	2.48	4.16
10	1.21	2.97	4.79

Table B.7: Capacitance of coplanar plates with and without fringing fields.

Table B.7 gives calculated capacitances for various W/S ratios. From Table B.7 it is apparent that a simple parallel plate approximation is not very good and that fringing fields should be included. The effect of fringing fields is given by:

$$C_f = C_0 \left[1 + \frac{S'}{\pi W'} \ln \left(\frac{\pi e W'}{S'} \right) \right] \text{[48, pp. 1245-1247]} \qquad \text{(B.48)}$$

where C_0 is the capacitance without fringing fields.
Values of C_f for various W/S ratios are also given in Table B.7. On the TPGD the ohmic output contact has a total length of 2.3 mm and an expected capacitance of 0.61 pF, as the ohmic contact width to separation ratio is 2/3.

B.4 Response Time

The response time of the detector is determined by the length of time it takes to drift the signal charge from the point of incidence to the ohmic output contact. This time is given by the collection time:

$$t_c = \int_i^f \frac{d\vec{l}}{v_d(E(\vec{r}))} \qquad \text{(B.49)}$$

where

l is the path taken for the initial point, i to the output ohmic contact, f, and

v_d is the drift velocity (a function of the electric field).

The path will be approximated by path perpendicular to the surface and one parallel to the surface along the electron potential minimum near the substrate/epi interface. For both sections, the drift velocity is taken as being 1×10^7 cm/s. This approximation is valid for the depletion fields expected in 1×10^{14} material and for a drift field of 1.33 kV/cm (4 volts between drift electrodes). The maximum drift length is 200 μm in the TPGD giving a maximum collection time of ≈ 2 ns. This is the time required to collect all electrons produced by ionizing radiation once the electric field re-establishes itself. The holes will begin to arrive immediately after production at the Schottky electrodes, and continue to arrive for 2 ns (assuming a saturation velocity of 1×10^6 cm/s). The hole signal will be capacitively coupled to the ohmic output contact, resulting in a pulse with a rise time of 2 ns (although the electrons will arrive with a spread of ≈ 0.22 ns, the total risetime will be governed by the velocity of the holes). The shape of the rising slope will depend on where the particle strikes the pixel. As the rise times of the amplifiers used with the TPGD are greater than the pulse rise time, its shape could not be observed. For a description of pulses shapes, see reference [11, Chapter3, Section 2]

B.5 Noise Sources

The noise from three sources was calculated and the sources compared.

B.5.1 Johnson noise

Johnson noise depends on the capacitance of the device in that this capacitance forms a filtering circuit with resistances in the circuit. Considering an idealized leaky capacitor detector as in Figure 6.21, the Johnson noise can be found by integrating:

$$\overline{V^2(f)}\, df = 4kTR\, df \tag{B.50}$$

over all frequencies. When convolved with the low pass filter that the detector can be represented as,

$$\begin{aligned}\overline{V^2(f)} &= \int_0^\infty \frac{\overline{V^2(f)}df}{1+\omega^2C^2R^2} \\ &= \frac{2kT}{\pi}\int_0^\infty \frac{R\,d\omega}{1+\omega^2C^2R^2} \\ &= \frac{2kT}{\pi C}\int_0^\infty \frac{dx}{1+x^2} \\ &= \frac{kT}{C}\end{aligned} \tag{B.51}$$

In terms of equivalent charge, the Johnson noise is given by:

$$N_J = C\sqrt{\overline{V^2}}/e = 400\sqrt{C} \qquad (C \text{ in pF}) \tag{B.52}$$

at 300 K.

B.5.2 Dark Current

The dark current (reverse leakage current through a p-n junction) is given by:

$$J_{dark} = \frac{en_{minor}}{\sqrt{\tau_r}}\left(\frac{kT}{q}\mu\right)^{\frac{1}{2}} \tag{B.53}$$

where n_{minor} is the minority carrier density, given by $n_{minor} = n_i^2/n_{major}$. Hence $J_{dark} = 9.5 \times 10^{-16}$ A/cm^2 = 0.95 fA/cm^2.

B.5.3 Generation Current

The generation current (current produced by thermally generated electrons and holes) is given by:

$$\begin{aligned}J_G &= \frac{ewn_i}{2\tau_r} \\ &= 32 \text{ nA/cm}^2\end{aligned} \tag{B.54}$$

where, for worst case,

$\tau_r = 1 \times 10^{-8}$ s,

$w = 20\mu$m,

$n_i = 2 \times 10^6$ cm^{-3}

This is considerably greater than the dark current and the dark current will be neglected.

The equivalent noise charge due to the generation current will be the total generation rate times the carrier transit time, t_c (all generation events are independent).

$$N_c = \frac{n_i\,d\,t_c}{\tau_r} = 800 \quad \text{cm}^{-2} \tag{B.55}$$

So for a pixel with dimensions of 2000 μm $\times 360\mu$m $\times 20\mu$m;

$$\begin{aligned} N_J &= 400\sqrt{C} \\ &= 400 \times \sqrt{0.61} \\ &= 315 \\ N_c &= 800 \times 360 \times 10^{-4} \times 0.2 \\ &= 6 \end{aligned}$$

Hence the noise is essentially entirely Johnson noise. Noise due to surface leakage currents can not be calculated, but is generally larger than any other noise source.

The signal produced by the passage of minimum ionizing radiation through 20 μm of GaAs is 3000 ehp giving a calculated signal-to-noise of 9 if all the charge is collected at one output contact and none is lost to traps or recombination centers. With transit times < 2 ns, trapping may on may not be a problem (minority carrier lifetime is > 10 ns).

B.6 Straggling

When a particle passing through a media deposits energy, it is assumed to do so through a series of random events [1], in each of which the particle loses an average energy of δE. As the collisions are random the number of collisions per unit path length follows a Poisson distribution with a standard deviation of $\sqrt{N(\delta r)}$. Hence the energy deposited per unit length also follows a Poisson distribution. Integrating over the entire path length through the media then results in a variation in the energy deposited given by the square root of the average energy loss.

B.7 Pion Energy Deposition

Pions with a momentum of 292 MeV/c (kinetic energy of 180 MeV) are minimum ionizing [44] and will have a stopping power of 6.8 MeV/cm. Thus they will lose 14 keV of energy passing through the 20 μm epitaxial layer. Protons with the same momentum (kinetic energy of 43.1 MeV) are not minimum ionizing and have a stopping power of 50.54 MeV/cm [44]. At this rate they will lose 101 keV in the epitaxial layer of the TPGD.

Bibliography

[1] R.D. Evans. *The Atomic Nucleus.* McGraw-Hill Book Company, Toronto, 1955.

[2] Glenn F. Knoll. *Radiation Detection and Measurement.* John Wiley & Sons, Toronto, 1979.

[3] E. Sakai. Present status of room temperature semiconductor detectors. *Nuclear Instruments and Methods*, 196(1):121–130, 1982.

[4] G.A. Armantrout, S.P. Swierkovski, J.W. Shersham, and J.H. Yee. What can be expected from high-Z semiconductor detection? *IEEE Transactions on Nuclear Science*, NS-24(1):121, 1977.

[5] G. Bertolini, F. Cappellani, and G. Restelli. Current state of the art in semiconductor detectors. *Nuclear Instruments and Methods*, 112:219–228, 1973.

[6] R. Zuleeg and K. Lehovec. Radiation effects in GaAs junction field effect transistors. *IEEE Transactions on Nuclear Science*, NS-27(5):1343–1354, 1980.

[7] Mayrant Simons. Radiation effects in GaAs integrated circuits: A comparison with silicon. *GaAs IC Symposium*, page 124, 1983.

[8] Victor A.J. van Lint. The physics of radiation damage in particle detectors. *Nuclear Instruments and Methods*, A253:453–459, 1987.

[9] K.Hesse, W.Gramann, and D.Hoppner. Room temperature GaAs gamma detector. *Nuclear Instruments and Methods*, 101:39–42, 1972.

[10] J.E. Eberhardt, R.D. Ryan, and A.J. Tavendale. Evaluation of epitaxial n-GaAs for nuclear radiation detector. *Nuclear Instruments and Methods*, 94:463–476, 1971.

[11] G. Bertolini and A. Coche, editors. *Semiconductor Detectors.* John Wiley & Sons, Inc., New York, 1968.

[12] F.B. McLean and T.R. Oldham. Charge funneling in n- and p-type Si substrates. *IEEE Transactions on Nuclear Science*, NS-29(6):2018–2023, 1982.

[13] R.M. Gilbert G.K. Ovrebo and J. Schifano. Plasma screening of funnel fields. *IEEE Transactions on Nuclear Science*, NS-32(6):4098–4103, 1985.

[14] Micheal Shur, Kang Lee, Robert Choe, and Erik Berger. Charge collection by drift during single particle upset. *IEEE Transactions on Nuclear Science*, NS-33(5):1140–1146, 1986.

[15] R.N. Hall. Recombination processes in semiconductors. *Proceedings of the IEE (London)*, B106(Suppl. 17):923–931, March 1960.

[16] M.A. Hopkins and J.R. Srour. Measurements of alpha-particle-induced charge in GaAs devices. *IEEE Transactions on Nuclear Science*, NS-30(6):4457–4463, 1983.

[17] Frank Stern. Calculated spectral dependence of gain in excited GaAs. *Journal of Applied Physics*, 47(12):5382–5386, December 1976.

[18] R. Boltz (Cominco), January 1987. Private communication.

[19] S.M. Sze. *Physics of Semiconductor Devices.* John Wiley & Sons, Toronto, second edition, 1981.

[20] Z. Shanfield, M.M. Moriwaki, W.M. Digby, and J.R. Srour. Characteristics of SEU current transients and collected charge in GaAs and Si devices. *IEEE Transactions on Nuclear Science*, NS-32(6):4104–4109, 1985.

[21] Emilio Gatti and Pavel Rehak. Semiconductor drift chamber - an application of a novel charge transport scheme. *Nuclear Instruments and Methods*, 225:608–614, 1984.

[22] Emilio Gatti, Pavel Rehak, and Jack T. Walton. Silicon drift chambers - first results and optimum processing of signals. *Nuclear Instruments and Methods*, 226:129–141, 1984.

[23] Pavel Rehak, Emilio Gatti, Antonio Longoni, J. Kemmer, Peter Holl, Robert Klanner, Gerhard Lutz, and Andrew Wylie. Semiconductor drift chambers for position and energy measurements. *Nuclear Instruments and Methods*, A235:224–234, 1985.

[24] J. Kemmer, G. Lutz, E. Belau, U. Prechtel, and W. Welser. Low capacity drift diode. *Nuclear Instruments and Methods*, A253:378–381, 1987.

[25] Ira Deyhimy, Richard C. Eden, and Jr. James S. Harris. GaAs and related heterojunction charge-coupled devices. *IEEE Transactions on Electron Devices*, ED-27(6):1172–1180, 1980.

[26] E.H. Rhoderick. Metal-semiconductor contacts. *IEE Proceedings*, 129(1):1–14, February 1982. Part 1.

[27] B.L. Sharma, editor. *Metal-Semiconductor Schottky Barrier Junctions and Their Applications*. Plenum Press, New York, N.Y., 1984.

[28] Marc Cuzin. Some new developments in the field of high atomic number materials. *Nuclear Instruments and Methods*, A253:407–417, 1987.

[29] David G. Webster. Detector design considerations. TRIUMF design note, October 1986.

[30] Corrie Kost and Fred Jones. RELAX3D: a FORTRAN program to solve the 3 dimensional Poisson (Laplace) equation. Technical report, TRIUMF Computing Services, 4004 Wesbrook Mall, Vancouver, B.C., V6T 2A3, February 1987.

[31] Maurice LeNoble. *Granular Metal Schottky Gallium Arsenide Charge Coupled Devices*. PhD thesis, University of British Columbia, 1988. In process.

[32] Greg R. Smith. The STAR online data acquisition system. Technical report, TRIUMF, 4004 Wesbrook Mall, Vancouver, B.C., V6T 2A3, July 1987.

[33] XELOSS. A program to calculate energy losses of particles in various materials using an iterative method.

[34] U. Littmark and J.F. Ziegler. *Handbook of Range Distributions for Energetic Ions in All Elements*, volume 6 of *The Stopping and Ranges of Ions in Matter*. Pergamon Press, New York, 1980.

[35] Ortec. *Instruments for Research Catalog 1002*. EG&G Ortec, 100 Midland Road, Oak Ridge, Tennessee, 1970.

[36] C.R. Gruhn. A thin epitaxial silicon detector with internal amplification. *IEEE Transactions on Nuclear Science*, NS-23(1):145–152, 1976.

[37] M.A. Hopkins and J.R. Srour. Charge collection measurements on GaAs devices fabricated on semi-insulating substrates. *IEEE Transactions on Nuclear Science*,

NS-31(6):1116–1120, 1984.

[38] Ronald S. Wagner, Jeffrey M. Bradley, Nicole Bordes, Carl J. Maggiore, Dipen N. Sinha, and Robert B. Hammond. Transient measurements of ultrafast charge collection in semiconductor diodes. *IEEE Transactions on Nuclear Science*, NS-34(6):1240–1245, 1987.

[39] John N. Bradford. Nonequilibrium effects in VLSI. *IEEE Transactions on Nuclear Science*, NS-25(5):1144–1145, 1978.

[40] E. L. Mathie, editor. *TRIUMF Users Handbook.* TRIUMF, Vancouver, B.C., Canada, 1987.

[41] E. H. Rhoderick. *Metal-Semiconductor Contacts.* Clarendon Press, Oxford, 1978.

[42] John Bardeen. Surface states and rectification at a metal semi-conductor contact. *Physical Review*, 71(10):717, 1947.

[43] V.L. Rideout. A review of the theory and technology for ohmic contacts to group III-V compound semiconductors. *Solid-State Electronics*, 18:541–550, 1975.

[44] L. G. Greeniaus. *TRIUMF Kinematics Handbook.* TRIUMF, Vancouver, B.C., Canada, second edition, September 1987.

[45] C.J. Wu and D. B. Wittry. Investigation of minority-carrier diffusion lengths by electron bombardment of Schottky barriers. *Journal of Applied Physics*, 49(5):2827–2836, 1978.

[46] P.A. Tove. Review of semiconductor detectors for nuclear radiation. *Sensors and Actuators*, 5:103–117, 1984.

[47] Phil Bennett and Corrie Kost. Opdata user's guide. Technical Report TRI-CD-87-04 Ver. 2.9, TRIUMF, 4004 Wesbrook Mall, Vancouver, B.C., V6T 2A3, July 1987.

[48] Philip M. Morse and Herman Feshbach. *Methods of Theoretical Physics.* McGraw-Hill Book Company, Inc., Toronto, 1953. Part II.